Ultraluminous high-redshift quasars from SkyMapper – II. New quasars and the bright end of the luminosity function

Christopher A. Onken, Christian Wolf, Fuyan Bian, Xiaohui Fan, Wei Jeat Hon, David Raithel, Patrick Tisserand

Monthly Notices of the ROYAL ASTRONOMICAL SOCIETY

MNRAS **511,** 572–594 (2022) https://doi.org/10.1093/mnras/stac051
Advance Access publication 2022 January 10

Ultraluminous high-redshift quasars from SkyMapper – II. New quasars and the bright end of the luminosity function

Christopher A. Onken [1,2★] Christian Wolf [1,2★] Fuyan Bian [3] Xiaohui Fan [4] Wei Jeat Hon,[5] David Raithel,[1] Patrick Tisserand [6] and Samuel Lai [1]

[1]*Research School of Astronomy and Astrophysics, Australian National University, Canberra, ACT 2611, Australia*
[2]*Centre for Gravitational Astrophysics, Australian National University, Canberra, ACT 2600, Australia*
[3]*European Southern Observatory, Alonso de Córdova 3107, Vitacura, Santiago 19, Casilla 19001, Chile*
[4]*Steward Observatory, University of Arizona, 933 North Cherry Avenue, Tucson, AZ 85721, USA*
[5]*School of Physics, University of Melbourne, Parkville, Victoria 3010, Australia*
[6]*Sorbonne Universités, UPMC Univ Paris 6 et CNRS, Institut d'Astrophysique de Paris, 98 bis bd Arago, F-75014 Paris, France*

Accepted 2022 January 6. Received 2022 January 5; in original form 2021 May 25

ABSTRACT

We search for ultraluminous Quasi-Stellar Objects (QSOs) at high redshift using photometry from the SkyMapper Southern Survey Data Release 3 (DR3), in combination with 2MASS, VHS DR6, VIKING DR5, AllWISE, and CatWISE2020, as well as parallaxes and proper motions from *Gaia* DR2 and eDR3. We report 142 newly discovered Southern QSOs at $3.8 < z < 5.5$, of which 126 have $M_{145} < -27$ AB mag and are found in a search area of 14 486 deg^2. This Southern sample, utilizing the *Gaia* astrometry to offset wider photometric colour criteria, achieves unprecedented completeness for an ultraluminous QSO search at high redshift. In combination with already known QSOs, we construct a sample that is >80 per cent complete for $M_{145} < -27.33$ AB mag at $z = 4.7$ and for $M_{145} < -27.73$ AB mag at $z = 5.4$. We derive the bright end of the QSO luminosity function at rest frame 145 nm for $z = 4.7$–5.4 and measure its slope to be $\beta = -3.60 \pm 0.37$ and $\beta = -3.38 \pm 0.32$ for two different estimates of the faint-end QSO density adopted from the literature. We also present the first $z \sim 5$ QSO luminosity function at rest frame 300 nm.

Key words: galaxies: active – quasars: general – early Universe.

1 INTRODUCTION

Supermassive black holes can be observed across vast distances, provided they accrete matter at a sufficient rate. Radiation released in the accretion process makes these objects the most luminous in the entire Universe. As long as they are not obscured by local dust, they will be seen as Quasi-Stellar Objects (QSOs) with characteristic spectral signatures. Ultraluminous QSOs point us to the most massive and fastest growing black holes in the Universe. The demographics of this type of object are of particular interest at high redshift, an era in the early universe in which black holes undergo their most dramatic and least-explained growth.

As these most extreme objects are intrinsically rare, any search for them has always been for the proverbial needles in a haystack. Over the last two decades, useful samples of high-redshift ultraluminous QSOs have been detected, supported by a range of massive data sets including the iconic Sloan Digital Sky Survey (SDSS; York et al. 2000), and later supported by all-sky data from the Widefield Infrared Survey Explorer (*WISE*; Wright et al. 2010). Two more useful steps have been the recent addition of a Southern analogue to SDSS, the SkyMapper Southern Survey (SMSS; Wolf et al. 2018a; Onken et al. 2019) as well as infrared sky surveys such as the VISTA Hemisphere Survey (VHS; McMahon et al. 2013). At all steps in this journey, candidate lists for the rare high-redshift QSOs were swamped with the tails of the distribution from cool, red stars in our own Milky Way Galaxy. A major simplification of these searches was delivered by the *Gaia* satellite mission (Gaia Collaboration 2018) of the European Space Agency (ESA); *Gaia* measured proper motions and parallaxes for a billion objects. This data set revealed the cool-star nature for a large fraction of the candidates, allowing effective cleaning of the candidate lists. Within two days of the release of *Gaia* DR2, Wolf et al. (2018b) identified the most luminous known QSO, SMSS J215728.21−360215.1 (a.k.a. SMSS J2157−3602) at $z = 4.692$, which has since been shown to be powered by a supermassive black hole with 34 billion solar masses (Onken et al. 2020).

As ultraluminous QSOs at high redshift are extremely rare, the size and completeness of a sample matters for any inference on the bright end of their luminosity function, their evolution with cosmic time in the early universe, their contribution to reionization in the early universe, and the evolution of their host galaxies and early galaxies in general. These objects also lend a helping hand to studies of the intergalactic medium and the build-up of chemical elements traced with absorption lines in foreground galaxies (Ryan-Weber et al. 2009; Simcoe et al. 2011). For all these reasons, enlarging the existing samples is a worthwhile undertaking.

Currently, the best reference for the bright end of the QSO luminosity function (LF) at redshift ∼5 is the work by Yang et al. (2016, hereafter Y16), which is based on a QSO sample from Wang

★ E-mail: christopher.onken@anu.edu.au (CAO); christian.wolf@anu.edu.au (CW)

et al. (2016, hereafter W16). Although various other works in the literature have updated the $z \sim 5$ QSO LF (e.g. McGreer et al. 2018; Kim et al. 2020; Niida et al. 2020), progress in this area is currently focused on the persistent uncertainties at the faint end. At the bright end, the exploitation of new data sources such as Pan-STARRS (Chambers et al. 2016) led to the discovery of many new QSOs (Schindler et al. 2019a; Yang et al. 2019), but no updates to the LF bright-end parameters. The work by Y16 inherited from its data source, the SDSS, a focus on the Northern hemisphere, and searching in the South offers an opportunity to at least double the sample and refine the sparsely populated bright end of the LF.

Hence, we had set out to discover ultraluminous high-redshift QSOs in the Southern sky, armed with a combination of the SMSS, the AllWISE data set[1] and *Gaia* DR2. The new *Gaia* data allowed Wolf et al. (2020, hereafter Paper I) to push QSO colour selection criteria closer to the main stellar locus, relative to the work by W16 and Y16, given that most stars could be identified and removed from the list by proper motions. The extended colour selections then revealed the rare QSOs with higher completeness than before. Similarly, Calderone et al. (2019) found that searches for QSO at all redshifts based on machine learning benefit from the *Gaia* data.

Paper I published a sample of 21 bright $z > 4$ QSOs, selected from SMSS DR2 with $i_{\rm PSF} < 18.2$ AB mag. In this paper, we extend the search with SMSS DR3, reaching deeper in magnitude and lower in Galactic latitude, and purify the selection by adding JHK photometry from VHS and the VIKING Survey (Edge et al. 2013), filling in data from the shallower 2 Micron All-Sky Survey (2MASS; Skrutskie et al. 2006) where needed. We present the results of our spectroscopic follow-up of candidates down to $z_{\rm PSF} \approx 19$ AB mag. We examine our evolving selection criteria in light of known high-redshift QSOs in the Southern sky and suggest selection rules going forward. We compare the results of our search to previous campaigns in the Northern sky, and provide an update to the bright end of the high-redshift QSO luminosity function in the often quoted rest frame 145-nm band. Finally, we present, for the first time, direct measurements for the bright end of the luminosity function at rest frame 300 nm.

Section 2 describes the data sources from which we construct our set of QSO candidates. In Section 3, we discuss properties of the known QSOs and the selection rules we adopt. In Section 4, we describe our spectroscopic follow-up of candidates, present the list of high-redshift QSOs we found, and discuss the completeness of the current sample. In Section 5, we construct luminosity functions and examine their evolution. Throughout the paper, we use Vega magnitudes for *Gaia* and IR data, and AB magnitudes for the SkyMapper passbands: *griz*. We adopt a flat ΛCDM cosmology with $\Omega_{\rm m} = 0.3$ and a Hubble–Lemaître constant of $H_0 = 70\,{\rm km\,s^{-1}\,Mpc^{-1}}$.

2 SEARCH AREA AND DATA SOURCES

We start from the `master` catalogue[2] of SMSS DR3, which covers nearly all the sky at declination $\delta < +2^\circ$; missing parts are primarily found very close to the Galactic plane and the Galactic Centre. In this work, we avoid areas with high object density, where photometry may be challenging, and high reddening, where high-redshift QSOs may be dimmed beyond our search depth. Hence, we focus on Galactic latitudes $|b| > 15^\circ$. These two simple geometric rules define an area that covers 38.35 per cent of the full sky, or 15 821 deg^2.

[1]Explanatory Supplement to AllWISE Data Release, http://wise2.ipac.caltech.edu/docs/release/allwise/expsup.
[2]See https://skymapper.anu.edu.au for catalogue details.

We further exclude specific areas: by default, bright stars in DR3 are surrounded by exclusion zones (for details see Onken et al. 2019), where detected sources are flagged and prevented from inclusion in the `master` table. For this work, the exclusion zones in z-band are relevant, which add up to 134 deg^2 within the search area. We also exclude areas around nearby galaxies, where, e.g. red supergiants and long-period variable stars can contaminate the QSO candidate list. We use the Updated Nearby Galaxy Catalogue (Karachentsev, Makarov & Kaisina 2013) of 869 galaxies from the Local Volume, and mask the sky within 1.3× the major angular diameter a_{26} (which corresponds to the Holmberg isophote of ∼26.5 mag(Vega) arcsec^{-2} in the B band) of all the galaxies. The largest resulting exclusion zones are around the LMC and SMC with 6.99 and 4.12 deg radius, respectively, as well as the region around the core of Sgr dSph that reaches to $|b| > 15^\circ$. All further galaxies have exclusion zones smaller than 0.5 deg, with the Sculptor dwarf galaxy, NGC 55, NGC 253 and Centaurus A being the next largest objects. The total excluded area is 276.5 deg^2.

We then select objects in the SkyMapper z-band, which has an effective mean wavelength of 916 nm and a FWHM of 84 nm. The bandpass efficiency curve is asymmetric as it rises steeply at the blue edge but rolls off to the red with the declining sensitivity of the CCD detectors (see Bessell et al. 2011). We limit the candidate selection to $z_{\rm PSF} < 19.5$ AB mag, although source incompleteness sets in at $z_{\rm PSF} \gtrsim 18.5$ AB mag, with a dependence on sky location originating from the SMSS progress as of DR3. Magnitude dependence of the incompleteness is discussed in detail below (Section 4.2.3).

From this SMSS DR3 list, we then use position-based cross-matches to other large-area surveys, such as those from *Gaia*, *WISE*, and VISTA. As new versions of the *WISE* and *Gaia* data sets were released in 2020 December, we replaced the AllWISE photometry for the *W*1 and *W*2 bands with the CatWISE2020 catalogue (hereafter CatWISE; Marocco et al. 2021), which is more precise for non-variable objects; with the release of *Gaia* eDR3 (Gaia Collaboration 2021), we updated our original selection from *Gaia* DR2 in order to further reduce our candidate lists with improved parallax and proper motion (PPM) information.

Using cross-matches with *Gaia* eDR3 contained in the DR3 `master` table, we consider objects where the nearest *Gaia* source is within 0.5 arcsec, and the second-nearest is at least 5 arcsec away. Close pairs of sources in *Gaia* often appear as one single SMSS source, causing the primary match to be more than 0.5 arcsec offset and showing a secondary match within 1–2 arcsec. Neighbours within 5 arcsec may affect the *WISE* photometry, given a *WISE* *W*1/*W*2 PSF with ∼6 arcsec FWHM, which would be detrimental to separating QSOs from cool stars. We require that *Gaia* has PPM data for the source and that the SMSS DR3 z-band photometry flags are < 4 (indicating reliable measurements). We estimate the fractional loss of objects due to these requirements by considering all known QSOs from the Milliquas v7.1 catalogue (Flesch 2015) in our search area that have $z > 3$ and $z_{\rm PSF} = 16$–19 AB mag. We find that we lose 6 per cent of objects, mostly due to the requirement of no neighbour being present within 5 arcsec. At this point, we end up with an effective search area of 35.1 per cent of the full sky, or 14 486 deg^2.

Then we take advantage of cross-matches between the SMSS `master` table and each of AllWISE and CatWISE, using only matches within 2 arcsec. Not all DR3 objects have a counterpart, but all known QSOs at $z > 4$ with $z_{\rm PSF} < 19$ AB mag do so. Marocco et al. (2021) quote the 90 per cent completeness depth for CatWISE as $W1 = 17.7$ mag and $W2 = 17.5$ mag. To examine the impact on our QSO search, we estimate the mean expected z-band magnitude of $z \sim 5$ QSOs at the *W*2 completeness limit from the average

colour of bright ($W2 < 15$ mag) known $z \sim 5$ QSOs, which is $z_{\rm PSF} - W2 \approx 3.75$. Hence, at $W2 = 17.5$ mag we expect $z_{\rm PSF} \approx 21.25$ AB mag, which exceeds the depth of our planned search by ∼2 mag. Brighter DR3 objects without *WISE* matches are most likely stars and not QSOs, because cool stars have bluer optical-minus-MIR colours. We also use data from the $W3$ band where it is available, but we do not require it for selection, because the 5σ sensitivity of $W3 = 11.3$ mag is too shallow for our purposes. Overall, we assume that the *WISE* data introduces no incompleteness into the high-redshift QSOs selection. In contrast, Y16 did find ALLWISE-imposed incompleteness to be important; however, such constraints only appeared at fainter magnitudes than are relevant for our search ($W1 > 17$ mag, $W2 > 16$ mag).

We note that about 6 per cent of $z > 4$ QSOs from Milliquas v7.1 lack a CatWISE entry, although all of them are present in AllWISE. Thus, we use CatWISE data where available and fill in AllWISE data where needed. As the $W1 - W2$ colour has been found useful for separating QSOs from cool stars and is also used in this work, we compared this colour for QSOs between AllWISE and CatWISE. We found the quoted uncertainties in $W1 - W2$ to shrink by a factor of 2.3 and the colour changes per object from AllWISE to CatWISE to be statistically consistent with the errors quoted in AllWISE. We also find that the colour range of high-redshift QSOs shrinks slightly, in line with the quoted error properties, although this test has only moderate significance given the small numbers of objects.

3 CANDIDATE SELECTION

In this section, we discuss the properties of known QSOs brighter than $z_{\rm PSF} = 19$ AB mag at redshift 4–6. We include all known QSOs in our search area, as listed in Milliquas v7.1, which includes QSOs published until 2021 Feb 14.[3] Based on the distribution of these known objects, we propose selection criteria for high-redshift QSOs that we assume to be complete except for rare cases with unusual colours. The sample of candidates resulting from these criteria has not been observed completely with spectroscopy but can inform future observations and the completeness of the verified samples.

3.1 PPM information from *Gaia*

Gaia eDR3 provides measurements of the parallax π, the proper motion μ_α, μ_δ, and their errors σ_π, σ_α, and σ_δ for most objects. For QSOs, we demand that these are all consistent with zero within the errors. We calculate a χ^2-style measure of consistency using

$$SN_{\rm PPM} = \sqrt{\frac{1}{3}\left(\left(\frac{\max(0,\pi)}{\sigma_\pi}\right)^2 + \left(\frac{\mu_\alpha}{\sigma_\alpha}\right)^2 + \left(\frac{\mu_\delta}{\sigma_\delta}\right)^2\right)}. \quad (1)$$

Our survey footprint contains 137 QSOs known before this work at magnitude $z_{\rm PSF} < 19$ AB mag and redshift $z \geq 4$. Of these, 132 objects (96 per cent) have $SN_{\rm PPM} < 2$ and 88 (64 per cent) have $SN_{\rm PPM} < 1$, in excellent agreement with the statistics expected for a population without parallax and proper motion. We also find no noticeable trend in the PPM properties with magnitude or redshift, which all lends high credibility to the quoted *Gaia* PPM measurement uncertainties.

[3]While this paper was under review, new releases of Milliquas (up to v7.3c on 28 Nov 2021) added 24 new QSOs discovered by other groups with confirmed redshifts between 4 and 6, mostly from Wenzl et al. (2021). However, only three are both in our search area and have $z_{\rm PSF} < 19$ AB mag; two were unconfirmed at the time of observation and are reported as 'discoveries' in our sample, as indicated in Table 3, and the third has $z_{\rm PSF} = 18.9$ AB mag, at which depth our spectroscopic follow-up remains incomplete.

3.2 Photometric information

Altogether, we consider the following photometric data: from SMSS DR3, the PSF magnitudes in the passbands *griz* (for full filter information, see Wolf et al. 2018a) as well as photometric flag information; from *Gaia* eDR3, the passbands G, B_p, and R_p, as well as the Bp/Rp Excess Factor; from VHS DR6 and VIKING DR5, the near-infrared passbands *JHK*; from CatWISE, the mid-infrared passbands $W1$ and $W2$; and from AllWISE, the passband $W3$. We correct the colours for interstellar foreground reddening using the extinction map from Schlegel, Finkbeiner & Davis (1998, hereafter SFD) with extinction coefficients for *Gaia* from Casagrande & VandenBerg (2018) for use in $A_{\rm band} = R_{\rm band} \times 0.86 \times E(B-V)_{\rm SFD}$ and for SkyMapper from Wolf et al. (2018a) for use in $A_{\rm band} = R_{\rm band} \times E(B-V)_{\rm SFD}$, as the Schlafly & Finkbeiner (2011) correction factor 0.86 is already absorbed into the extinction coefficients. In the NIR, we had chosen $(A_J, A_H, A_K) = (0.8, 0.5, 0.3) \times 0.86E(B-V)$, which is a little different from the values (0.75, 0.41, 0.24) suggested by Wang & Chen (2019), but the effects are mostly on the order of 0.01 mag in the low-reddening areas we are searching. We assume no extinction in the *WISE* passbands.

First we address an issue with *Gaia* photometry of faint red sources: in Fig. 1, we show the Bp/Rp Excess Factor and the colours $G - R_p$ and $B_p - R_p$ versus G magnitude of all QSOs known in the search area within a narrow redshift range of $4.7 < z < 5.3$. While there is no trend of $G - R_p$ colour with brightness in G, there is a strong trend of $B_p - R_p$ getting bluer and the Excess Factor increasing as the magnitude gets fainter. Riello et al. (2021) discuss the origin of this bias towards higher B_p fluxes in red objects that are near the detection limit in the B_p channel. Here, we attempt to rectify the $B_p - R_p$ colour with an ad hoc quadratic correction, only for objects with $G > 19$ mag, of the form

$$B_{p,\rm c} - R_p = B_p - R_p + 0.3 \times (\max(0, G - 19))^2 \,. \quad (2)$$

The right-hand panel in the figure shows the result of this correction, and in the following we adopt such corrected $B_{p,\rm c} - R_p$ colours.

Fig. 2 shows the redshift trends of several colour indices formed from the passband measurements and corrected for foreground reddening. We see well-known features:

(i) Strong trends of colour with redshift arise as the spectral step from the unabsorbed QSO continuum to the Ly α forest near $\lambda_{\rm rest} \simeq 120$ nm is redshifted through the spectral range, see e.g. $G - R_p$, $B_{p,\rm c} - R_p$, $G - r_{\rm PSF}$, $g_{\rm PSF} - r_{\rm PSF}$, and $r_{\rm PSF} - i_{\rm PSF}$.

(ii) Where both passbands in a colour index probe unabsorbed continuum, it reflects the spectral slope of the continuum, which has only moderate scatter in the bulk of the QSO population, see e.g. $z_{\rm PSF} - J$, $J - K$, and $K - W1$.

(iii) Emission lines vary colours slightly as they are redshifted through the passbands, most notably the strong line H α in the colours $K - W1$ and $W1 - W2$, where variations with redshift trace the structured passband efficiency curve of $W1$.

3.3 QSO selection criteria

Based on the distribution of colours observed for the existing QSO sample, we propose the following set of selection criteria to define

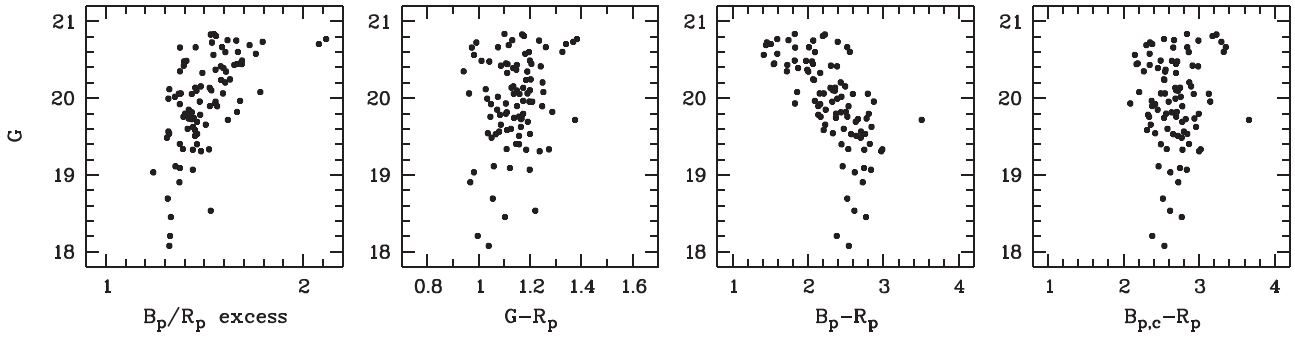

Figure 1. *Gaia* photometry of redshift $4.7 < z < 5.3$ QSOs near the faint end, where little flux is expected in the B_p channel, while the G band and the R_p channel should still see significant flux: the B_p/R_p Excess Factor increases from a value of ∼1.3, which is typical for point sources of this colour, to values around 2 near the detection limit (left-hand panel); the $G - R_p$ colour shows no trend with magnitude (centre-left), but the $B_p - R_p$ colour drifts bluewards towards the detection limit (centre right), suggesting extra flux being recorded. We use the ad hoc quadratic correction from equation (2) to rectify the B_p bias (right-hand panel).

the volume of QSO candidates at $z \geq 4.4$:

$$\begin{array}{lll} 0.8 < & G - R_p & < 1.8 \\ 1.8 < & B_{p,c} - R_p & \\ 0.9 < & g_{\rm PSF} - r_{\rm PSF} & \text{if measured} \\ 0.7 < & J - K & < 1.8 \\ 1.5 < & J - W1 & < 3 \\ 0.2 < & W1 - W2 & < 1.1 \\ 2.3 < & W1 - W3 & < 4.7 \quad \text{if measured} \end{array} \tag{3}$$

We further define three indices, i_1, i_2, and i_3, to reduce the contamination from broad absorption line QSOs (BALQSOs) at $z < 4$ and from distant cool stars:

$$\begin{array}{lll} 0 < & (J - K) + (B_{p,c} - R_p) - (z_{\rm PSF} - J) - 1.8 & = i_1 \\ 0 < & (J - W1) - 1.4(z_{\rm PSF} - J) + 0.1 & = i_2 \\ 0 < & 0.6 - 0.5(r_{\rm PSF} - i_{\rm PSF}) - (G - r_{\rm PSF}) & = i_3. \end{array} \tag{4}$$

We include objects that are undetected in r band. Considering the colour trends with redshift, it would seem reasonable to make stronger use of the $r_{\rm PSF} - i_{\rm PSF}$ colour. Unfortunately, this requires r-band data at the depth of the SMSS Main Survey, but in DR3 the hemisphere is only complete with deep data in i band and z band, while deep r band covers only two thirds of the hemisphere. A non-detection in r band may thus be either a sign of high redshift or a sign of shallow data, depending on the sky position. Hence, we do not attempt to fully exploit the r-band information at this stage.

Compared to the distribution of sources in Fig. 2, the $G - R_p$ colour limit of 1.8 mag is rather conservative. The adopted boundary was motivated by the existence of five $z > 4$ sources from Milliquas v7.1 that fall within the range of 1.5–1.8 mag, although none have parallax measurements in *Gaia* eDR3.

Finally, we apply a cut in PPM significance (see equation 1):

$$SN_{\rm PPM} < 2\,, \tag{5}$$

which should make us lose only around 4 per cent of the QSO sample, while keeping contamination by Milky Way stars low.

These simple geometric selection rules may seem suboptimal, as several authors have convincingly argued that other techniques – a general Bayesian selection (e.g. Wolf, Meisenheimer & Röser 2001; Richards et al. 2009; Mortlock et al. 2012; Reed et al. 2017), or machine learning approaches (e.g. Calderone et al. 2019; Guarneri et al. 2021; Wenzl et al. 2021) – ought to be superior in modelling the amorphous locus of QSOs in high-dimensional spectral energy distribution (SED) space. However, previous QSO samples at high redshift were incomplete, with a highly structured selection function, which we do not want to propagate into our study. After all, this work aims at improving the completeness of observed samples. Hence, we chose not to apply elaborate statistical methods to inferior training samples when informing our follow-up observations.

The final candidate list within our selection volume includes 197 objects brighter than $z_{\rm PSF} = 18.7$ AB mag. Of these, 64 were known QSOs as of Milliquas v7.1, with 17 reported by Wolf et al. (2018b) and Paper I, and a further 47 reported by a variety of authors including W16, Yang et al. (2017), Schindler et al. (2019a), Yang et al. (2019), and Lyke et al. (2020). This left 133 new candidates with $z_{\rm PSF} < 18.7$ AB mag to be followed up. The list includes a further 497 fainter candidates with $z_{\rm PSF} \gtrsim 18.7$ AB mag, of which 21 were known QSOs as of Milliquas v7.1, leaving 476 candidates to follow up in this and future work.

3.4 Spectroscopic follow-up

This work builds on the study of Paper I and extends it to fainter magnitudes from SMSS DR3. We have followed up 132 of the 133 unstudied objects from our $z_{\rm PSF} < 18.7$ AB mag candidate list. Also, we followed up 154 fainter objects that extend to $z_{\rm PSF} \simeq 19$ AB mag, about 1 mag deeper than Paper I.

We note that during the early phase of this work, we had not yet applied the faint correction to the *Gaia* B_p magnitudes mentioned in Section 3.2. At that stage, we had additional candidates with $B_p - R_p > 1.8$ mag but $B_{p,c} - R_p < 1.8$ mag, a small number of which we have followed up, as shown by the black points outside the selection cut in the $B_{p,c} - R_p$ panel of Fig. 2. These objects, however, did not end up in our complete sample discussed later, as they were all in the incomplete redshift range at $z < 4.4$.

In addition, we have pursued a complementary search by occasionally sampling objects outside our selection criteria, in order to explore whether we are missing an unknown QSO population at high redshift. However, the only high-redshift QSO discovered this way was one at $z = 4.39$, whose colours were indeed all within the selection criteria, while its PPM signal was slightly larger than our cutoff.

4 SPECTROSCOPY AT THE ANU 2.3-M TELESCOPE: 2017–2021

We have used the Wide Field Spectrograph (WiFeS; Dopita et al. 2010) on the ANU 2.3-m telescope at Siding Spring Observatory

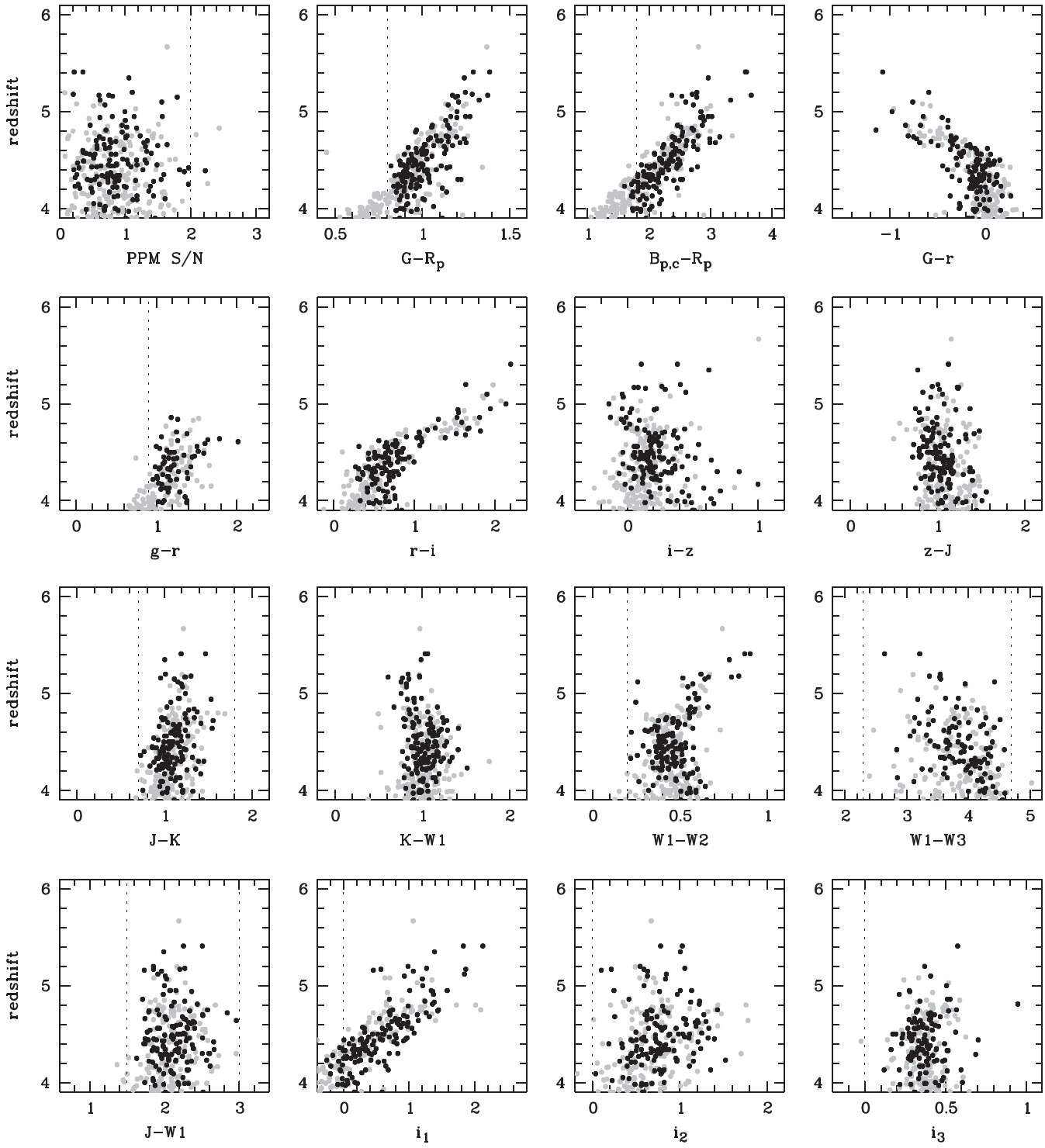

Figure 2. Characteristics of known high-redshift QSOs with $z_{PSF} < 19$ AB mag at redshift $z > 3.9$: significance of parallax and proper motion signal (top left) and colour indices (all other panels). Grey points are previously known QSOs and black points are new objects presented in this work. Dashed lines indicate the adopted selection criteria, which eliminate only four of the QSOs at $z \geq 4.4$. The colour indices i_1, i_2, and i_3 are defined in equation (4). A few of the $z < 4.4$ QSOs discovered in this work were inside the selection criteria before we corrected the faint *Gaia* B_p magnitudes as explained in Section 3.2.

for a number of nights between 2017 December and 2021 October. In conjunction with the standard RT560 beam-splitter, we primarily used the WiFeS B3000 and R3000 gratings in the blue and red arm, respectively, which together cover the wavelength range from 360 to 980 nm at a resolution of $R = 3000$. This setup allows us to see QSO spectra from the Ly α forest to the C IV line for all objects at redshift $z < 5$. At redshift $z > 5$, the C IV line starts to get lost in the sky noise and for the highest-redshift objects it is even outside the data range. However, in these cases the Ly α forest, in combination with the Ly α and Si IV line, are sufficient to confirm objects as high-redshift

QSOs. Because of mechanical issues with the instrument, two nights used alternative gratings in the red arm: I7000 in 2020 December and R7000 in 2021 April. Despite the restricted wavelength range in each case, numerous candidates were successfully classified. Exposure times ranged from 600 to 2 400 s, and observing conditions varied in terms of cloud cover and seeing. For the faintest objects, we obtained and co-added two spectra of up to 2 400 s each.

The data were reduced using the Python-based pipeline PyWiFeS (Childress et al. 2014). PyWiFeS calibrates the raw data with bias, arc, wire, internal-flat and sky-flat frames, and performs flux calibration and telluric correction with standard star spectra. Flux densities were calibrated using a number of standard stars, which are usually observed on the same night, although not necessarily under the same cloud conditions.[4] We then extracted spectra from the calibrated 3D data cube using QFitsView.[5] Reduced spectra were visualized with the MARZ software (Hinton et al. 2016) and template spectra were overplotted to aid the classification and redshift determination. We estimate redshifts from broad Si IV, N V, and C IV lines where available, and consider the blue edge of the Ly α line when necessary. Because of frequent absorption within the emission line profiles and the possibility of C IV blueshifts, we determined the redshifts manually, and thus we estimate that the redshift uncertainties range from 0.01 to ∼0.05 for weak-lined objects.

Since 2017 December, spectra were taken for 739 objects, of which 577 provided sufficient signal for a confident classification. Most of the targets are not candidates anymore after using the refined PPM data of *Gaia* eDR3. 252 targets were observed to be QSOs, 67 per cent of which are at $z > 3.8$. (Among those 170 QSOs were seven discovered by other groups and mistakenly included in our observing lists.) QSOs at lower redshift include objects with red continua as well as extreme BALQSOs and overlapping iron trough low-ionization BALQSOs (OFeLoBALQSOs), which mimic the optical colours of high-redshift QSOs, but have MIR colours typical of their redshift, hence we have learned how they can largely be avoided from the start. Several stars contaminated the candidate lists, especially before the *Gaia* eDR3 release. Altogether 13 stars turned out to be likely red supergiants in nearby galaxies including NGC 300, the Sculptor and Fornax dwarf galaxies, the SMC and LMC, and later we chose to exclude the sky areas covered by these.

4.1 Newly identified high-redshift QSOs

Among the 197 candidates defined by the final selection criteria in the nearly complete magnitude range at $z_{\rm PSF} < 18.7$ AB mag, there are 116 $z \geq 4$ QSOs, 29 (mostly BAL) QSOs at $z < 4$ and 19 stars. The remaining objects are not high-redshift QSOs, although we cannot type them confidently, either due to low signal in the spectra or due to unusual spectral features. As described in Section 4.2.1, only 4 known high-redshift QSOs were excluded by these criteria.

In Tables 1–3, we report our 142 newly identified high-redshift QSOs, split into three redshift ranges. Of these, 126 QSOs are more luminous than $M_{145} = -27$. The highest redshift objects are at $z = 5.41$, and together with the objects from Paper I, the total number of $z > 3.8$ QSOs discovered with this project is 163, of which 90 per cent have $M_{145} < -27$ AB mag.

The tables list z-band AB and H-band Vega magnitudes, which are useful for the LF construction and for planning more detailed follow-up observations.[6] In many cases, the H-band magnitude is not observed but inferred from J and K magnitudes, or if necessary, from the $z_{\rm PSF}$ and $W1$ photometry. We use the mean colour relations that we find in the sample, which are $H - K = 0.41(J - K)$ and $H - W1 = -0.007 + 0.4677(z_{\rm PSF} - W1)$. The relations are roughly linear across colour, with a root mean square (RMS) scatter of 0.1 mag and 0.15 mag, respectively, and have no trend with redshift in our range of concern.

4.2 Completeness considerations

In this section, we explore how to define a complete sample for use in the luminosity functions. Our selection criteria were adopted to provide a complete sample of QSOs at redshift $z \geq 4.4$, at least to a depth of $z_{\rm PSF} \approx 19$ AB mag. At fainter magnitudes, the uncertainties in colours broaden the QSO distribution and the significance of the PPM information degrades, making our approach less effective.

4.2.1 Colour and PPM selection effects

Currently, there are 143 QSOs known in our search area with $z \geq 4.4$ and $z_{\rm PSF} < 19$ AB mag. Here, we have assumed that all literature QSOs within these limits are contained in the compilation Milliquas v7.3 (Flesch 2015). Of the known QSOs, four objects are rejected by the selection criteria of Section 3.3: two because of the PPM signal and two more because of their colours. One additional known $z = 4.87$ QSO is nearly blended with a cool star and thus eliminated by our requirement for no close neighbours, which has reduced our effective search area. Hence, we conclude that our PPM and colour selection criteria may miss ∼3 per cent of the candidates across our search area of 14 486 deg^2.

While considering the known QSOs implies that we inherit traditional selection biases, we note that we were able to relax and extend the selection beyond previous rules, because the *Gaia* PPM data vastly reduced the stellar contamination. The majority of objects in the sample considered here are new QSOs identified using our extended cuts. By considering our selection boundaries relative to the shape of the QSO distributions against colour in Fig. 2, we see that we capture not only the bulk of the QSO population but also its tails, and that the remaining incompleteness based on the photometric selection cuts must be small.

4.2.2 Upper redshift limit?

While we make no attempt to avoid the detection of QSOs at the highest possible redshifts, we assume that our search is only complete to $z \simeq 5.4$, where we find our two highest redshift objects. Inspecting Fig. 3 suggests that the sample is conspicuously devoid of bright QSOs at $z > 5.5$.

[4]This lack of robust flux calibration precludes an independent estimation of the absolute magnitudes from the spectroscopy.
[5]https://www.mpe.mpg.de/~ott/QFitsView/

[6]One faint source in Table 2 has no z-band photometry in SMSS DR3, and here we substituted the photometry from the NOIRLab Source Catalog (NSC) DR2 (Nidever et al. 2021). We have been unable to locate any NIR photometry for the source, but the lack of an M_{300} estimate does not affect our analysis, because it falls well below the brightness regime in which we are complete and from which we construct the LFs.

Table 1. List of newly discovered QSOs. Redshift $3.8 \leq z < 4.4$; these are not part of a complete sample and are hence not used for the luminosity functions. Epoch is the date of the first spectrum taken by us. Comments refer to non-standard observing setups or unusual properties. See Appendix A for the spectra.

SMSS ID	Redshift	R_p (Vega)	$z_{\rm PSF}$ (AB)	H (Vega)	$W1$ (Vega)	$W1-W2$ (Vega)	M_{145} (AB)	M_{300} (AB)	Epoch (spectrum)	Comments
J000458.11−213044.7	4.09	18.365	18.28	16.14 ± 0.04	14.58	0.27	−27.56	−28.50	20191128	
J000948.16–371708.1	4.27	17.679	17.95	16.41 ± 0.04	15.02	0.45	−27.97	−28.31	20201208	
J003222.03−035807.5	4.12	18.318	18.49	16.84 ± 0.04	15.30	0.48	−27.40	−27.83	20201209	I7000
J005938.27−422704.1	4.25	18.463	18.69	17.26 ± 0.03	15.77	0.51	−27.21	−27.45	20201208	
J010201.12–211545.9	4.29	18.281	18.40	16.60 ± 0.04	15.12	0.40	−27.53	−28.12	20191023	
J014615.01–635639.2	4.28	17.695	18.14	16.33 ± 0.04	14.96	0.48	−27.80	−28.39	20200926	
J021218.22–394548.8	4.13	17.222	17.46	15.62 ± 0.03	13.99	0.38	−28.39	−29.04	20201209	I7000
J021638.50–033737.8	4.31	18.546	18.81	17.01 ± 0.04	15.44	0.52	−27.14	−27.72	20201001	
J022654.20–322924.0	4.30	18.973	18.78	16.51 ± 0.01	14.80	0.52	−27.15	−28.21	20210118	
J024535.48–445433.0	4.02	18.027	17.93	16.07 ± 0.03	14.82	0.56	−27.88	−28.55	20190703	
J030427.83–780559.2	4.00	18.400	18.57	16.71 ± 0.05	15.18	0.59	−27.36	−27.95	20210118	
J034132.56–411920.9	4.30	18.940	18.68	16.45 ± 0.04	14.65	0.51	−27.25	−28.28	20200927	
J042529.68–395805.8	4.36	18.890	19.05	17.54 ± 0.08	16.17	0.54	−26.93	−27.46	20200810	
J043802.34–530028.9	4.21	18.563	18.71	16.67 ± 0.02	15.00	0.39	−27.17	−28.02	20210203	
J045459.29–420742.6	4.17	19.398	18.96	16.97 ± 0.04	15.19	0.56	−26.91	−27.70	20211022	
J045623.58–085248.5	3.90	18.676	18.49	16.14 ± 0.04	14.44	0.65	−27.30	−28.44	20191130	
J045639.34–402753.6	4.18	18.087	18.38	16.61 ± 0.04	15.21	0.57	−27.51	−28.08	20201209	I7000
J052439.12–304800.4	4.17	18.052	18.40	16.66 ± 0.05	15.36	0.53	−27.48	−28.02	20201209	I7000
J055901.33–855138.3	3.90	18.986	18.61	16.76 ± 0.06	15.35	0.51	−27.24	−27.85	20200927	
J061751.60–240610.8	4.09	18.413	18.59	17.05 ± 0.10	15.61	0.62	−27.28	−27.61	20210118	
J083905.36–222215.9	4.30	18.423	18.51	16.63 ± 0.05	15.20	0.43	−27.52	−28.13	20200227	$b_{\rm gal} = 11\overset{\circ}{.}5$
J091926.16–094920.5	4.38	18.338	18.67	17.18 ± 0.07	15.74	0.39	−27.31	−27.57	20210411	R7000
J092623.99–261620.9	4.35	18.453	18.46	16.77 ± 0.06	15.04	0.47	−27.61	−28.01	20210306	
J095759.35–230941.8	4.32	18.451	18.60	16.68 ± 0.06	15.11	0.57	−27.39	−28.06	20210405	
J104046.17–294635.5	4.33	18.486	18.78	17.14 ± 0.09	15.64	0.40	−27.21	−27.61	20210407	
J110144.63–260043.5	4.37	18.682	18.78	16.98 ± 0.06	15.58	0.51	−27.24	−27.78	20210405	
J113649.79–161939.6	4.25	18.192	18.35	16.70 ± 0.05	15.32	0.40	−27.58	−28.02	20210307	
J120828.90–044419.9	4.33	18.642	18.74	17.20 ± 0.06	15.47	0.22	−27.22	−27.54	20210408	
J131656.26–301244.3	4.29	18.761	18.76	17.14 ± 0.09	15.69	0.34	−27.23	−27.60	20210408	
J132343.04–052951.6	4.04	18.174	18.27	16.61 ± 0.04	15.29	0.65	−27.57	−28.02	20210404	
J132626.48–341716.4	4.36	18.562	18.61	16.98 ± 0.07	15.53	0.26	−27.40	−27.78	20210410	
J134633.39–275654.3	3.97	18.678	18.49	16.85 ± 0.07	15.52	0.54	−27.35	−27.77	20210404	
J135729.80–234839.2	4.34	18.823	18.96	17.48 ± 0.08	16.14	0.37	−27.06	−27.28	20200627	
J151045.68–045007.4	4.05	18.903	18.76	16.66 ± 0.04	14.98	0.35	−27.14	−27.99	20210408	
J151904.00–095230.8	4.22	18.432	18.65	16.90 ± 0.05	15.60	0.60	−27.36	−27.84	20210409	
J155141.82–153448.9	4.33	18.230	18.21	16.46 ± 0.04	15.13	0.46	−27.94	−28.35	20200221	Weak-lined
J160013.90–112800.2	4.29	18.863	18.99	17.07 ± 0.07	15.50	0.47	−27.30	−27.78	20210704	
J164147.78–775029.8	4.13	18.090	17.88	16.19 ± 0.04	14.86	0.54	−28.14	−28.53	20200819	See Appendix B
J172847.61–643404.6	4.22	18.261	18.34	16.71 ± 0.05	15.17	0.44	−27.64	−28.02	20200926	
J181348.59–742305.6	4.33	18.547	18.59	17.02 ± 0.08	15.60	0.40	−27.50	−27.76	20200927	
J182616.06–474625.4	4.23	18.629	18.94	17.35 ± 0.11	15.78	0.43	−27.03	−27.38	20210703	
J185854.75–414702.1	4.34	18.762	18.97	16.75 ± 0.05	14.82	0.48	−27.07	−28.02	20210704	
J193603.72–702734.4	4.39	18.580	18.79	16.86 ± 0.06	15.15	0.46	−27.26	−27.92	20201001	
J194707.16–443732.3	4.13	18.876	18.82	17.32 ± 0.11	15.69	0.42	−27.09	−27.36	20210704	
J195455.50–222254.5	4.30	18.611	18.62	16.76 ± 0.05	14.88	0.52	−27.50	−28.04	20210411	
J201808.60–390820.6	4.10	18.701	18.40	16.70 ± 0.06	15.24	0.48	−27.48	−27.96	20201001	
J202712.66–245732.8	4.34	18.959	18.96	17.20 ± 0.07	15.75	0.37	−27.06	−27.55	20210711	
J202914.99–015504.0	4.23	18.630	18.86	17.31 ± 0.08	15.30	0.38	−27.20	−27.45	20210711	Extended?
J205659.53–513055.1	3.84	19.262	18.90	17.28 ± 0.06	15.73	0.53	−26.80	−27.26	20210711	
J214938.09–805805.1	4.22	18.987	18.86	16.99 ± 0.07	15.35	0.39	−27.23	−27.78	20201002	
J222820.62–422626.3	3.99	18.718	18.67	16.55 ± 0.04	15.00	0.51	−27.11	−28.05	20210711	
J230318.14–603123.8	4.35	18.136	18.52	16.82 ± 0.05	15.23	0.38	−27.44	−27.92	20201210	
J230513.15–031958.9	4.35	18.494	18.68	17.13 ± 0.05	15.77	0.39	−27.31	−27.62	20210711	
J230824.53–453905.6	3.99	18.640	18.65	16.83 ± 0.04	15.16	0.51	−27.12	−27.77	20210711	
J230857.62–500914.9	3.98	17.372	17.47	15.98 ± 0.01	14.41	0.59	−28.29	−28.61	20190904	
J231141.53–142215.7	3.98	18.571	18.29	16.26 ± 0.04	14.77	0.56	−27.51	−28.34	20210702	
J231500.34–364049.9	4.27	18.842	18.88	16.91 ± 0.05	15.32	0.47	−27.05	−27.81	20200627	
J232438.44–201956.9	4.23	18.285	18.58	16.94 ± 0.06	15.45	0.35	−27.34	−27.77	20200926	

Here, it is worth highlighting our reliance on *Gaia* data and the redshift constraints this imposes. Beyond redshift ∼5.5, very little flux remains in the *Gaia G* passband from which the astrometric measurements are made. In fact, none of the known QSOs beyond $z = 5.7$ have *Gaia* parallax measurements in eDR3. In the regime between $z = 5.4$ and $z = 5.7$, we expect the Ly α equivalent width to play an important role in determining whether *Gaia* can measure a parallax or proper motion.

Table 2. List of newly discovered QSOs. Redshift $4.4 \leq z < 4.7$ QSOs. One faint object has a z-band magnitude from the NOIRLab Source Catalogue (NSC) DR2. See also caption of Table 1.

SMSS ID	Redshift	R_p (Vega)	$z_{\rm PSF}$ (AB)	H (Vega)	$W1$ (Vega)	$W1-W2$ (Vega)	M_{145} (AB)	M_{300} (AB)	Epoch (spectrum)	Comments
J003438.57−762140.5	4.47	18.423	18.57	17.07 ± 0.07	15.59	0.38	−27.46	−27.73	20200627	
J003656.23–241844.1	4.62	18.414	18.52	16.89 ± 0.04	15.29	0.37	−27.49	−27.95	20191022	
J004022.28–333316.7	4.42	18.375	18.29	16.43 ± 0.01	14.94	0.51	−27.68	−28.32	20201208	
J004541.14–553511.9	4.45	18.149	18.35	17.04 ± 0.05	15.80	0.36	−27.61	−27.73	20201208	
J004917.31–081723.4	4.56	18.588	18.68	17.16 ± 0.07	15.81	0.40	−27.35	−27.66	20200630	
J010255.67–574246.3	4.56	18.252	18.44	16.84 ± 0.05	15.18	0.42	−27.55	−27.97	20200926	
J014423.70–114948.1	4.44	18.536	19.04	16.93 ± 0.11	15.10	0.44	−26.93	−27.46	20210711	z-band from NSC
J020348.61–231453.8	4.50	18.898	18.99	17.32 ± 0.06	15.72	0.39	−26.99	−27.47	20200701	
J024422.99–515931.6	4.46	18.779	19.12	17.36 ± 0.06	15.79	0.42	−26.86	−27.39	20200810	
J024622.42–603753.7	4.57	18.341	18.47	16.72 ± 0.04	15.28	0.43	−27.53	−28.09	20191023	
J025445.42–275042.5	4.54	18.628	18.67	17.29 ± 0.02	16.04	0.40	−27.32	−27.51	20211022	
J025629.33–402041.8	4.51	18.393	18.42	16.91 ± 0.04	15.35	0.38	−27.56	−27.88	20191023	
J030333.78–225121.4	4.57	18.662	18.85	17.05 ± 0.05	15.40	0.43	−27.14	−27.77	20200701	
J031139.48–404428.8	4.43	18.997	18.90	17.10 ± 0.06	15.72	0.47	−27.07	−27.66	20200701	
J032233.76–594328.1	4.42	18.546	18.77	16.91 ± 0.06	14.97	0.40	−27.21	−27.85	20191024	
J033951.43–473959.9	4.45	18.507	18.65	17.24 ± 0.04	15.63	0.40	−27.31	−27.52	20191024	
J034029.49–322353.9	4.66	18.925	19.07	17.33 ± 0.06	15.73	0.34	−26.95	−27.48	20200802	
J034342.87–155923.6	4.57	18.995	19.03	17.40 ± 0.07	15.98	0.30	−27.02	−27.55	20200810	
J034831.18–764305.5	4.66	18.617	18.62	16.93 ± 0.06	15.31	0.36	−27.50	−27.97	20200226	
J035647.24–122512.1	4.66	18.162	18.15	16.73 ± 0.06	15.53	0.36	−27.91	−28.14	20200630	
J044514.74–422805.6	4.48	18.949	19.01	17.28 ± 0.07	15.95	0.55	−26.96	−27.49	20200820	
J045926.71–443855.2	4.65	18.684	18.57	16.81 ± 0.04	15.45	0.49	−27.45	−28.04	20200120	
J051047.28–505722.5	4.44	18.890	18.75	17.22 ± 0.06	15.96	0.53	−27.22	−27.54	20210118	
J093037.26–321931.1	4.43	18.072	18.32	16.47 ± 0.04	14.85	0.43	−27.76	−28.33	20201209	$b_{\rm gal} = 13.^{\circ}7$, I7 000
J095735.42–263039.4	4.49	18.381	18.56	16.88 ± 0.07	15.43	0.46	−27.48	−27.92	20200621	
J104556.31–073145.9	4.47	18.684	18.84	17.09 ± 0.04	15.51	0.51	−27.15	−27.69	20200226	
J105124.18–114529.8	4.43	18.769	18.90	17.21 ± 0.03	15.83	0.49	−27.10	−27.56	20200227	
J105702.65–231013.7	4.50	18.325	18.33	16.75 ± 0.05	15.15	0.47	−27.68	−28.05	20200130	
J110948.79–222757.7	4.49	18.922	18.99	17.33 ± 0.08	15.95	0.53	−27.02	−27.46	20200621	
J114230.62–082330.6	4.46	19.145	18.97	17.00 ± 0.05	15.33	0.45	−27.03	−27.78	20200228	
J122749.22–300600.1	4.63	18.120	18.29	16.71 ± 0.06	14.98	0.34	−27.78	−28.16	20210403	
J125559.18−110812.7	4.56	18.671	18.93	17.19 ± 0.05	15.54	0.46	−27.09	−27.63	20200228	
J133821.00−245845.8	4.60	18.537	18.69	17.12 ± 0.07	15.51	0.22	−27.37	−27.74	20200228	
J134930.11−382208.4	4.40	18.815	18.89	17.18 ± 0.09	15.57	0.41	−27.15	−27.60	20200626	Redshift uncertain
J145904.70−160326.6	4.46	18.617	18.74	17.16 ± 0.03	15.48	0.29	−27.35	−27.64	20210408	Extended/multiple
J152219.16−271543.7	4.44	17.942	18.11	16.39 ± 0.05	15.02	0.38	−28.14	−28.47	20210404	
J181812.74−564925.1	4.62	19.106	19.09	17.47 ± 0.10	15.98	0.46	−27.03	−27.56	20200813	
J192427.57−582750.5	4.45	18.823	18.79	17.12 ± 0.08	15.78	0.44	−27.32	−27.70	20200616	
J210743.01−494803.3	4.48	19.027	19.20	17.61 ± 0.06	15.93	0.39	−26.80	−27.33	20200812	
J212109.58−404824.4	4.68	18.934	18.91	17.04 ± 0.05	15.48	0.53	−27.16	−27.84	20210711	
J212132.33−651825.6	4.40	19.057	19.19	17.71 ± 0.11	16.19	0.45	−26.80	−27.33	20200813	
J212358.26−391345.4	4.57	19.014	19.03	17.49 ± 0.10	16.00	0.23	−26.99	−27.52	20200812	
J220004.31−291438.6	4.62	18.617	18.79	17.18 ± 0.02	15.44	0.30	−27.23	−27.67	20200616	
J221150.10−525343.5	4.40	18.323	18.52	16.96 ± 0.04	15.67	0.32	−27.45	−27.79	20210702	
J221423.26−142456.0	4.62	19.082	19.14	17.41 ± 0.09	15.78	0.44	−26.91	−27.44	20200812	
J225551.95−122635.7	4.44	18.633	18.77	17.14 ± 0.06	15.82	0.58	−27.23	−27.63	20200630	
J231425.23−665057.9	4.47	19.064	19.08	17.29 ± 0.09	15.86	0.45	−26.91	−27.44	20200813	
J231614.93−461027.6	4.65	18.704	18.75	17.10 ± 0.04	15.51	0.38	−27.26	−27.76	20200627	
J232009.94−605703.5	4.58	18.773	18.67	17.27 ± 0.06	15.81	0.44	−27.33	−27.56	20210712	
J232518.43−584301.2	4.40	18.476	18.55	16.75 ± 0.02	15.63	0.36	−27.42	−27.99	20210119	
J234842.90−214749.0	4.45	18.256	18.43	16.60 ± 0.05	15.11	0.50	−27.56	−28.17	20200615	
J235834.56−493325.3	4.42	18.933	19.04	17.26 ± 0.03	15.64	0.35	−26.92	−27.45	20200627	

4.2.3 Incompleteness at the faint end

A significant consideration in this work is sample incompleteness at the faint end due to two different reasons: first, there is the source incompleteness of SMSS DR3, which we use as a parent sample. We use the z-band number counts of objects listed in our search area of DR3 and obtain a linear fit to the brightness range of $z_{\rm PSF} = 16$–19 AB mag. The downturn from the linear fit (with slope 0.254 ± 0.001) indicates the magnitude-dependent source incompleteness of the parent sample (left-hand panel in Fig. 4). We find that the completeness declines from 100 per cent at $z_{\rm PSF} = 17$ AB mag to 95 per cent at $z_{\rm PSF} = 18.5$ AB mag, to 86 per cent at $z_{\rm PSF} = 18.7$ AB mag, and to 63 per cent at $z_{\rm PSF} = 19$ AB mag. Secondly, the spectroscopic follow-up of the selected candidate list by the literature and by this work is only complete (bar one candidate)

Table 3. List of newly discovered QSOs. Redshift $4.7 \leq z < 5.5$ QSOs. 'W21' indicates two QSOs recently reported by Wenzl et al. (2021). See also caption of Table 1.

SMSS ID	Redshift	R_p (Vega)	z_{PSF} (AB)	H (Vega)	$W1$ (Vega)	$W1 - W2$ (Vega)	M_{145} (AB)	M_{300} (AB)	Epoch (spectrum)	Comments
J010924.31−503749.7	5.12	19.271	18.93	17.49 ± 0.05	16.18	0.26	−27.38	−27.55	20210929	
J012736.71−300649.6	4.73	18.909	19.11	17.17 ± 0.02	15.78	0.52	−26.97	−27.50	20200810	
J012938.99−582942.7	4.75	18.594	18.76	17.22 ± 0.05	15.88	0.56	−27.32	−27.68	20200120	
J014534.68−163950.3	4.71	18.497	18.49	16.85 ± 0.11	15.43	0.49	−27.57	−28.03	20191128	
J020240.11−294314.4	4.86	18.894	19.08	17.19 ± 0.02	15.80	0.55	−27.07	−27.75	20200818	
J020436.66−252315.2	4.86	18.249	18.53	16.59 ± 0.11	14.90	0.66	−27.63	−28.35	20191020	
J021739.31−125025.0	4.73	18.862	18.89	17.39 ± 0.07	16.17	0.42	−27.18	−27.50	20200630	
J022009.01−352745.3	5.07	18.942	18.91	17.30 ± 0.02	15.94	0.55	−27.38	−27.72	20211020	
J023648.56−114733.7	5.20	18.634	18.40	16.78 ± 0.04	15.51	0.62	−27.96	−28.29	20200926	
J024133.93−543853.0	4.74	18.723	18.89	17.40 ± 0.06	16.18	0.46	−27.21	−27.51	20200630	
J031431.12−573152.7	5.10	18.732	18.81	17.03 ± 0.05	15.71	0.57	−27.51	−28.00	20200801	
J032933.94−410056.1	4.83	18.596	18.62	17.07 ± 0.14	15.69	0.55	−27.51	−27.86	20200626	
J033703.05−254831.5	5.15	18.493	18.28	16.59 ± 0.04	15.27	0.64	−28.05	−28.46	20191128	z=5.08?
J035210.62−214544.9	5.16	19.012	18.86	17.02 ± 0.06	15.83	0.52	−27.52	−28.04	20211022	
J040732.95−281031.3	4.75	18.467	18.62	16.91 ± 0.04	15.11	0.43	−27.48	−27.99	20200120	
J050328.89−195623.0	5.00	18.316	18.46	16.62 ± 0.05	15.34	0.59	−27.81	−28.37	20210203	
J050928.30−183435.1	4.70	18.579	18.62	16.96 ± 0.05	15.62	0.46	−27.46	−27.93	20200820	
J082450.79−674241.5	5.41	18.775	18.72	16.64 ± 0.05	14.95	0.90	−27.85	−28.38	20210118	
J084347.76−253155.6	4.75	18.629	18.62	16.92 ± 0.06	15.53	0.41	−27.56	−28.01	20200119	$b_{gal} = 10.^{\circ}5$, W21
J113522.01−354838.8	4.95	18.407	18.23	16.72 ± 0.05	15.29	0.59	−28.08	−28.29	20190705	
J121921.12−360933.0	4.74	18.710	18.46	16.51 ± 0.05	14.88	0.46	−27.69	−28.41	20210203	
J162551.54−043049.4	5.17	18.659	18.68	16.54 ± 0.04	15.32	0.80	−27.90	−28.61	20210409	
J162758.93−083343.6	4.79	18.945	18.86	16.94 ± 0.05	15.46	0.56	−27.54	−28.08	20210704	
J165333.86−761426.1	5.41	18.423	18.20	16.31 ± 0.04	14.72	0.87	−28.33	−28.87	20200227	
J192600.92−314202.6	5.35	19.237	18.80	17.38 ± 0.08	15.95	0.78	−27.68	−27.79	20210703	
J194124.59−450023.6	5.18	18.488	18.22	16.45 ± 0.05	14.91	0.84	−28.20	−28.64	20200615	
J205559.20−601147.3	4.95	18.926	18.84	17.22 ± 0.05	15.73	0.55	−27.42	−27.76	20200616	
J211002.60−454548.3	4.80	18.878	19.17	17.46 ± 0.03	16.16	0.57	−26.96	−27.49	20200813	
J214608.20−485819.5	5.17	18.325	18.34	16.44 ± 0.02	14.88	0.66	−28.01	−28.63	20210429	
J223419.12−804013.3	4.91	18.941	18.75	17.22 ± 0.09	15.81	0.25	−27.58	−27.79	20210710	
J232952.75−200038.7	5.05	18.548	18.45	16.55 ± 0.05	14.95	0.65	−27.84	−28.46	20200625	W21
J233435.28−365708.8	4.72	19.165	18.92	16.51 ± 0.03	14.59	0.38	−27.13	−28.37	20200813	

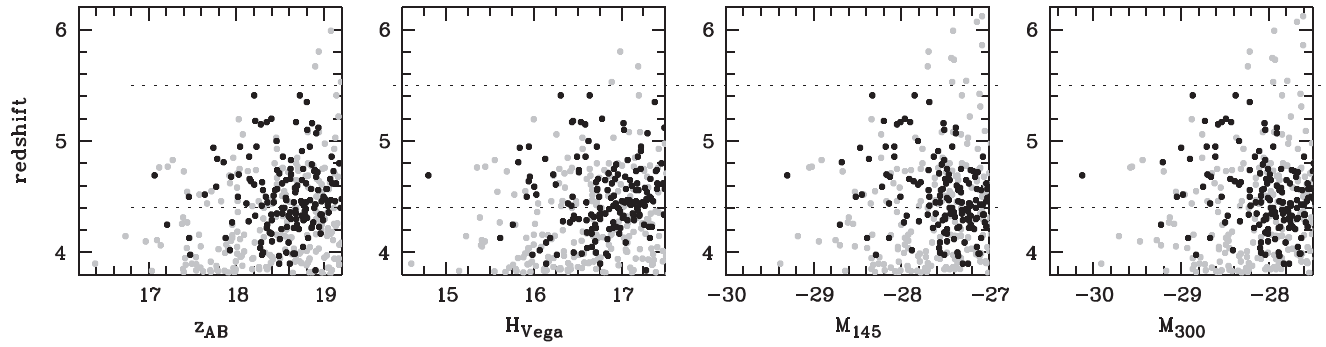

Figure 3. The current Southern bright high-redshift QSO sample: apparent optical and IR magnitude (left and centre-left panels) and luminosity at 145 nm and 300 nm (centre-right and right). Dark points are QSOs found with SkyMapper and reported by Wolf et al. (2018b), Paper I, and this work. Light points are QSOs from the literature in the search area targeted in this work. The relative lack of objects at redshift $z > 5.5$ suggests the sample is incomplete there.

to $z_{PSF} < 18.7$ AB mag; fainter than that, the completeness drops quickly to ∼30 per cent at $z_{PSF} \simeq 19$ AB mag (right-hand panel in Fig. 4).

Secondly, we use NIR photometry from the three surveys 2MASS, VHS, and VIKING, with a 2 arcsec matching radius. We find that 6 per cent of Milliquas QSOs with $z > 3$ and $z_{PSF} = 16$–19 AB mag have no *JK* data, which we showed in Section 3.3 as being helpful in selecting high-redshift QSOs. This affects mostly fainter QSOs without 2MASS counterparts, in areas where neither the deeper VHS nor the VIKING survey is available at present. At $z_{PSF} < 18$ AB mag this incompleteness amounts to 2 per cent, and reaches 7 per cent by $z_{PSF} = 18.7$ AB mag and ∼10 per cent by $z_{PSF} = 19$ AB mag.

In conclusion, we have a highly complete sample of $z = 4.4$–5.4 QSOs at $z_{PSF} < 18.7$ AB mag and a substantial further sample down to $z_{PSF} \simeq 19$ AB mag. The completeness at $z_{PSF} >$ 18.7 AB mag is difficult to estimate reliably given the interplay of source incompleteness in the parent sample, incompleteness in

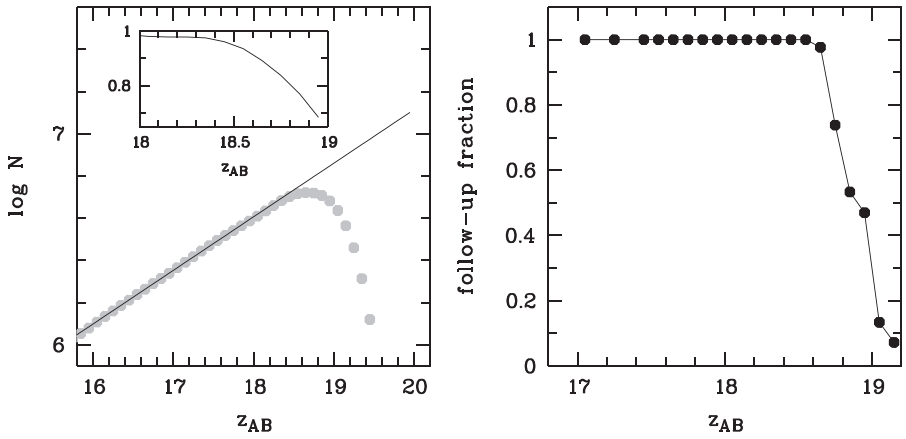

Figure 4. Completeness diagnostics: the SMSS z-band source list is incomplete at $z_{\rm PSF} > 18.5$ AB mag (left-hand panel), as diagnosed by the source number counts in the search area; the derived source completeness as shown in the inset declines from 95 per cent at $z_{\rm PSF} = 18.5$ AB mag to 63 per cent at $z_{\rm PSF} = 19$ AB mag. Starting from the source list, the spectroscopic follow-up is complete at $z_{\rm PSF} < 18.7$ AB mag, while completeness drops to ∼10 per cent at $z_{\rm PSF} = 19$ AB mag.

spectroscopic follow-up, and the fraction of true QSOs among the candidates, which will likely decline as we go fainter and contamination by non-QSOs in the candidate sample increases. We thus leave the faint-end incompleteness untreated in this work; further follow-up is progressing to find the missing QSOs at $z_{\rm PSF} > 18.7$ AB mag.

Cumulative number counts as a function of apparent magnitude (z and H band), split into two redshift ranges ($4.4 \leq z < 4.7$ and $4.7 \leq z < 5.4$; the latter selected to match that of Y16), are shown in the left-hand panels of Fig. 5.

4.3 Sample comparisons between North and South

We now want to ask whether the new sample in the Southern hemisphere and the established literature sample in the Northern hemisphere are statistically consistent. Therefore, we look specifically at the redshift range $4.7 < z < 5.4$ in our sample and compare it with the W16/Y16 sample in the same redshift range that was searched in a Northern area of similar size (within 1 per cent). The comparison between the cumulative number counts for this redshift range is shown in Fig. 5(E). Our sample is >80 per cent complete to $z_{\rm PSF} \simeq 18.7$ AB mag, where it contains 38 objects, compared to 25 objects in the Y16 sample (they have another 21 objects down to their spectroscopic completeness limit of $z_{\rm SDSS} = 19$ AB mag). This factor of ∼1.5 is easily explained by the different completeness of candidate selection: calculations by Y16 suggest that their candidate selection is 50–60 per cent complete, while we assume >80 per cent completeness for our sample. In contrast, the slight difference in the z bandpasses of SDSS and SkyMapper plays very little role: comparing the SDSS and SMSS z-band AB magnitudes for eight objects in common between Y16 and our Southern sample at $z_{\rm PSF} < 18.7$ AB mag, we find a mean $z_{\rm SDSS} - z_{\rm SMSS} = -0.01$ mag with an RMS of 0.14 mag.

Next, we ask whether the completeness of Y16 appears well-estimated in hindsight: we try to apply the selection cuts of Y16 to our sample and count what fraction of objects we lose. The largest difference in the selection is that Y16 require $W1 - W2 > 0.5$ mag, which was needed in the pre-*Gaia* era to combat the vast stellar contamination, while we relaxed the cut to $W1 - W2 > 0.2$ mag given *Gaia*'s PPM data. At $z_{\rm PSF} < 19$ AB mag, our inclusive selection rules revealed 55 QSOs, while using $W1 - W2 > 0.5$ mag retains 34 of these (62 per cent), in agreement with the original completeness correction used by Y16. Clearly, there are ultraluminous $z \sim 5$ QSOs waiting to be discovered in the Northern hemisphere using updated *WISE* colour cuts and *Gaia* data.

Among the QSOs selected by our criteria, there are 12 in the SDSS footprint, for which we can fully replicate the Y16 selection rules. We find only one object that the Y16 $W1 - W2$ colour cut would have retained, but which the other Y16 rules would exclude (SDSS J013127.34−032100.1). Although based on only one object, this suggests a possible, modest ∼10 per cent correction to the Y16 completeness, in addition to the *WISE*-based factor above.

4.4 Estimation of M_{145} and M_{300}

Because of (a) limited S/N and significant sky emission line residuals in the WiFeS spectra, (b) the frequent presence of BAL features blueward of C IV, and (c) the desire to compile a homogeneous dataset for the LF that includes QSOs from the literature, we estimate the QSO absolute magnitude at rest frame 145 nm, M_{145}, utilizing a composite spectrum of bright QSOs from $z = 1$–2 (Selsing et al. 2016, S16, hereafter). In comparison to other QSO composite spectra that incorporate lower luminosity objects (e.g. Vanden Berk et al. 2001; Telfer et al. 2002), the S16 composite[7] provides a better match to the low-equivalent-width QSOs that one typically finds at high luminosity (as expected from the Baldwin effect; Baldwin 1977; Rakshit, Stalin & Kotilainen 2020).

The S16 composite is convolved with the relevant filter curves to normalize the spectrum with the observed photometry. The z-band filter curves for SMSS and SDSS, and the H-band filter curve for VISTA were retrieved from the Spanish Virtual Observatory (SVO) Filter Profile Service[8] (Rodrigo, Solano & Bayo 2012; Rodrigo & Solano 2020).

We validated the application of the S16 composite by comparing the associated M_{145} predictions against the subsample of W16/Y16 data that was drawn from SDSS spectroscopy (in contrast to their

[7]Retrieved from https://github.com/jselsing/QuasarComposite.
[8]http://svo2.cab.inta-csic.es/theory/fps/

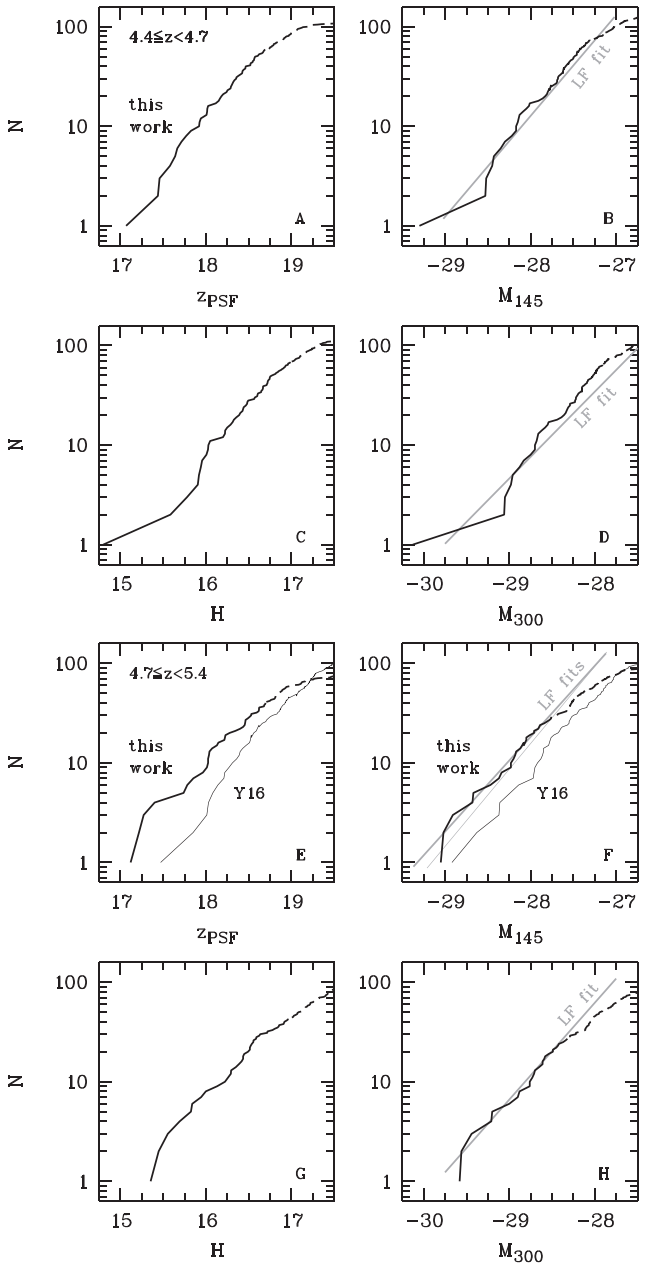

Figure 5. Cumulative QSO number counts versus apparent magnitude in z and H band (panels ACEG) and versus absolute magnitude M_{145} and M_{300} (panels BDFH). The top panels (ABCD) show $4.4 \leq z < 4.7$, while the bottom panels (EFGH) show $4.7 \leq z < 5.4$. The incomplete tail of our sample line is dashed. Panels E and F include a comparison with the Y16 sample. Thick grey lines are predictions from our luminosity function fits (the thin grey line in panel F is the Y16 fit, renormalized to our cosmology and area).

own follow-up data, calibrated from SDSS i-band photometry). From 52 QSOs, the median M_{145} difference, after adding 0.07 mag to the values from Y16,[9] was only 0.06 mag (with the S16 composite slightly brighter), with an RMS of just 0.12 mag. We take this as evidence that the combination of the observed photometry and the S16 composite spectrum will give robust results for computing the M_{145} LFs.[10]

For M_{300}, we apply a similar procedure, but based on the H-band photometry (measured or inferred). From the S16 composite, $M_{145} - M_{300} = 0.53$ mag, but extrapolating the M_{300} magnitudes from z band would typically produce a slightly brighter M_{300} value than our H-band-based estimates (up to 0.5 mag). This indicates that the spectral slopes of our QSOs are slightly bluer than the composite, as confirmed by the mean colour of the QSOs in our sample, $M_{145} - M_{300} = 0.38$ mag. The bluer colours are consistent with the findings of Xie et al. (2016), in which more luminous QSOs had bluer UV spectral slopes. However, by anchoring our M_{300} estimates to H band, we minimize any associated error arising from variations in the spectral slope.

Cumulative number counts for M_{145} and M_{300} are shown in the right-hand panels of Fig. 5, split into our two redshift ranges.

5 LUMINOSITY FUNCTIONS

At the bright end, the number counts in the Southern sample exceed the number counts used previously for deriving the luminosity function of high-redshift QSOs. This allows us to be less dependent on completeness corrections. Hence, we re-derive the luminosity function for the bright end and update estimates of the luminosity density and redshift evolution. Using the S16 composite spectrum, we can relate the apparent-magnitude completeness limit of $z_{PSF} = 18.7$ AB mag to a absolute-magnitude limit ranging from $M_{145} = -27.25$ AB mag at $z = 4.4$ to -27.73 AB mag at $z = 5.4$, and from $M_{300} \simeq -27.8$ AB mag at $z = 4.4$ to -28.3 AB mag at $z = 5.4$ (although we note that the M_{300} magnitudes used in the LF calculation are estimated from H band rather than extrapolating all the way from z band). In the half-magnitude bin fainter than $z_{PSF} = 18.7$ AB mag, the completeness of our sample collapses from >80 per cent to ∼10 per cent.

Prior to the application of any magnitude constraints, this final sample contains 171 QSOs in our search area of 14 486 deg^2, which is defined by $\delta < +2°$, $|b| > 15°$, and the exclusion zones detailed in Section 2. This sample excludes our two highest-redshift QSOs as well as a large number of QSOs identified at $z < 4.4$. One of the literature QSOs does not have z-band magnitude from SMSS DR3, and we use the value from NSC DR2 instead ($z = 18.68$ AB mag). The sample is assumed to be overall ∼95 per cent complete at $z_{PSF} < 18$ AB mag and >80 per cent at $z_{PSF} < 18.7$ AB mag, which we take into account for our statistical analysis.

For $4.4 \leq z < 4.7$, we have 54 QSOs brighter than $M_{145} = -27.33$ AB mag and which are used in the LF fitting below. That sample has a median redshift of 4.52. For the $4.7 \leq z < 5.4$ sample,

[9]The Y16 cosmological parameters ($\Omega_\Lambda = 0.728$) predict 3.3 per cent larger luminosity distances at $z = 5$ relative to ours.

[10]In Paper I (and the initial arXiv version of this work), our M_{145} estimates relied on simple interpolation between the SMSS i_{psf} and z_{psf} photometry. However, by ignoring the contributions of the UV emission lines, either photometric interpolation or the assumption of a fixed power-law continuum anchored to a single photometric band are likely to yield M_{145} estimates that are systematically too bright. In particular, over the redshift interval $z = 4.7$–5.4, the S16 composite gives M_{145} values between 0.12 and 0.25 mag fainter than suggested by a ($\alpha_\nu = -0.3$) power-law continuum anchored to z band. Recent work by Grazian et al. (2022) at $z \sim 5$ have used similar power-law estimates (anchored to SMSS i band), and our composite-based M_{145} values are, in the mean, 0.18 mag fainter for the same 14 objects. Such use of i-band is particularly fraught as the redshift increases above $z = 4.8$, where the flux through the filter is first boosted by Ly α emission, and then is soon diminished by Ly α absorption.

which covers the same redshift interval as Y16 (a median redshift of 4.83 versus 4.92 from Y16), we retain 28 QSOs brighter than $M_{145} = -27.73$ AB mag.

For the first time, NIR photometry yields direct measurements of M_{300} for a wide-area sample of QSOs at the bright end. This is due to the simultaneously deep and wide coverage of the VHS, which has no equivalent in the Northern hemisphere, where the samples for previous determinations of the bright end of the luminosity functions were found. Similar to our treatment of M_{145}, we apply cuts in M_{300} to define the samples for fitting the LFs. The thresholds of $M_{300} < -27.86$ and -28.26 AB mag for the low and high redshift bins, respectively, are the S16 equivalents for $z_{\rm PSF} = 18.7$ AB mag. As discussed in Section 4.4, because the spectral slopes of our QSOs are, on average, bluer than the S16 composite spectrum, the M_{300} thresholds we adopt from the z-band limit are conservative. None the less, we end up with similar numbers of QSOs in the M_{300} LF fits for our two redshift ranges: 49 and 30.

5.1 Parametric luminosity function fits

We compare our data with the best-fitting model of the LF from Y16, which is parametrized with a double power law as

$$\Phi(M, z) = \frac{\Phi^*(z)}{10^{0.4(\alpha+1)(M-M^*)} + 10^{0.4(\beta+1)(M-M^*)}}, \quad (6)$$

having a turnover in the density centred at luminosity $M^* = -26.98 \pm 0.23$ AB mag, a faint-end slope of $\alpha = -2.03$ and a bright-end slope of $\beta = -3.58 \pm 0.24$. The normalization, in units of number mag^{-1} Mpc^{-3}, is taken to evolve as $\log_{10}\Phi^*(z) = -8.82 - 0.47(z - 6)$ (Fan et al. 2001), and we evaluate it at the median redshifts of our two bins. As noted in Section 4.4, we also add 0.07 mag to the M^* value from Y16 and adjust their comoving volume, as their cosmological parameters predict larger luminosity distances at $z = 5$. The incompleteness of the Southern sample at the faint end is evident as a slope change in the right-hand panels of Fig. 5, particularly in the higher redshift bin.

To fit the LF, we adopt a Maximum Likelihood approach like that used by Y16 (see Marshall et al. 1983). We incorporate our full completeness model and consider two recent versions of the $z \sim 5$ faint-end LF: those of Niida et al. (2020) and Kim et al. (2020), hereafter N20 and K20, respectively. To probe such faint regimes, both surveys naturally covered much smaller areas, 340 and 85 deg^2, respectively, which yielded 72 and 32 QSOs across the M_{145} range of -23 to -27 AB mag.[11] We take their respective faint-end slopes and normalizations, and fit our bright QSO sample (28 QSOs) with the double power law of equation (5.1). For each of the two faint-end models, we allow M^* to vary as part of the fit, but adjust Φ^* in a manner that maintains the existing fit to the faint-end data, given their respective α parameters. In this way, we fit β and M^*, but also recompute Φ^*.

First, we utilised the N20 faint-end parameters, namely $\alpha = -2.00$ and a faint-end normalization that remains consistent with their combination of $\log_{10}\Phi^* = -8.26$ mag^{-1} Mpc^{-3} for $M^* = -27.15$ AB mag. (N20 fixed their bright-end slope based on a fit to Y16 and McGreer et al. (2013), but utilised an independent selection of bright QSOs from SDSS DR7 in their MLE fit.) We adopted the redshift evolution of Φ^* from Fan et al. (2001) to scale the normalization from their mean redshift of $z = 4.75$ to our mean redshift of 4.91. With our bright-end data, we then derive $\beta = -3.60 \pm 0.37$ and $M^* = -27.09 \pm 0.30$ ABmag, which gives $\log_{10}\Phi^* = -8.32$ mag^{-1} Mpc^{-3}.

We then performed a similar fit with the K20 parameters, i.e. $\alpha = -1.11$ and $\log_{10}\Phi^* = -7.35$ mag^{-1} Mpc^{-3} for $M^* = -25.81$ AB mag at $<z> = 4.95$. (In contrast to N20, K20 explicitly used the Y16 data to constrain the bright end in their MLE fit.) We find $\beta = -3.38 \pm 0.32$ and $M^* = -25.87 \pm 0.33$ AB mag, implying $\log_{10}\Phi^* = -7.33$ mag^{-1} Mpc^{-3}.

The results from fitting with each faint-end constraint are provided in Table 4, and the bright-end LFs are overplotted as straight lines in panels (B) and (F) of Fig. 5 (using the parameters from the K20 faint end). We also plot the Y16 LF fit in Fig. 5(F), where we have scaled their parameters to our cosmology and to our search area.

The overall $z \sim 5$ LF shape is illustrated in Fig. 6, with the prior results shown in thin lines, and the new fits shown in thick lines for high redshift (solid) and low redshift (dashed). For the N20 parameters, there is some tension with the QSO densities found at the faint end of our highly complete survey region, where the close proximity between M^* and our faint-end cutoff of -27.73 AB mag results in a steeper bright-end slope. In contrast, the shallower slope of K20 (in conjunction with its high normalization) has no direct impact on the bright-end fit, and M^* is more than 1 mag fainter, well below our sample's completeness limit.

While the LF in the low-redshift bin is generally higher at all magnitudes, the steeper bright-end slopes may suggest a change in behaviour at the brightest magnitudes (see Section 5.2).

Previous work, principally based on the Y16 sample, found broadly similar slopes, with data-driven 'best' free fits ranging from $\beta = -3.94$ by N20 and $\beta = -3.80$ by Y16 to $\beta = -3.50$ by K20. At a slightly lower redshift of $z \sim 3.9$, Boutsia et al. (2021) found a similar bright-end slope of $\beta = -4.0^{+0.6}_{-0.4}$. The Extremely Luminous QSO Survey (ELQS; Schindler et al. 2019b) found bright-end slopes for the redshift range of $2.8 < z < 4.5$ in the range from $\beta = -4$ to -4.5 depending on the details of the fitting boundaries.

For the M_{300} LF at $z \sim 5$, we lack the deep H-band photometric data to provide the counterparts to the N20 and K20 constraints, so we focus on fitting just a single power law to the bright end of the LF. Applying the same MLE technique to that above, we fit the LF as a pure power law. Retaining the redshift dependence of Fan et al. (2001) for the LF normalization, we fit the β and Φ values at $M_{145} = -28.5$ AB mag at $z = 4.4$–4.7, and $M_{145} = -28.75$ AB mag at $z = 4.7$–5.4.

At $z = 4.4$–4.7, from 49 QSOs, we find the best fit to the bright end of the M_{300} LF to be $\beta = -3.18 \pm 0.22$ and $\log_{10}\Phi(M_{300} = -28.5) = -9.18 \pm 0.05$ mag^{-1} Mpc^{-3}. In the $z = 4.7$–5.4 bin, from 30 QSOs, we find $\beta = -3.43 \pm 0.32$ and

Table 4. Restframe 145 nm LF parameters for double power-law.

Median z	β	M^*	α	$\log_{10}\Phi^*$
	Faint-end constraints from Kim et al. (2020)			
4.52	-3.53 ± 0.24	-26.02 ± 0.18	-1.11	-7.17
4.83	-3.38 ± 0.32	-25.87 ± 0.33	-1.11	-7.33
	Faint-end constraints from Niida et al. (2020)			
4.52	-3.92 ± 0.32	-27.32 ± 0.13	-2.00	-8.24
4.83	-3.60 ± 0.37	-27.09 ± 0.30	-2.00	-8.32

[11] As illustrated by Harikane et al. (2022), at the faint end of the N20 and K20 absolute magnitude ranges, the population of UV sources is rapidly transitioning from being QSO-dominated to being galaxy-dominated, so contamination in the QSO samples becomes a serious concern.

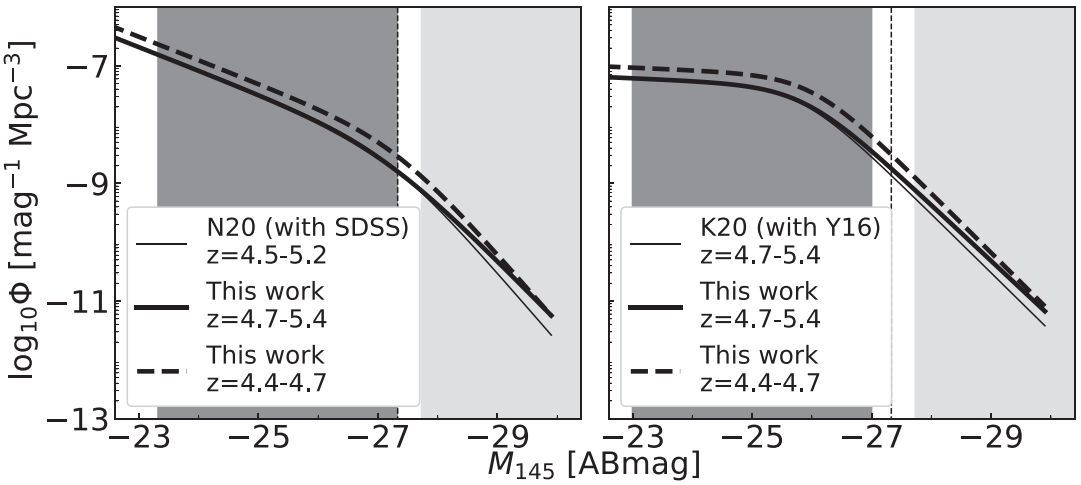

Figure 6. Parametrized QSO LF models at $z \sim 5$, combining our bright-end data with the faint-end slopes and normalizations of (*left*) N20 and (*right*) K20. The solid lines show the fits at $z = 4.7$–5.4: ours (thick), and the original N20/K20 models (thin). The bright-end fitting regions for our data are shown in the light grey shaded areas for $z = 4.7$–5.4. Our fits to the $z = 4.4$–4.7 sample are shown with thick dashed lines and the lower magnitude bounds for $z = 4.4$–4.7 are shown as vertical dotted lines. The fits include sources up to a maximum of $M_{145} = -29.1$ AB mag. The faint-end samples cover the dark grey regions of $M_{145} \sim -23$ to ~ -27 AB mag.

$\log_{10}\Phi(M_{300} = -28.75) = -9.56 \pm 0.06$ mag^{-1} Mpc^{-3}. The LF fits are shown with straight lines in panels (D) and (H) of Fig. 5.

We note that these two redshift bins suggest different directions of evolution in the bright-end slopes for M_{145} and M_{300} (flatter and steeper, respectively, towards higher z). However, at present, this comparison is limited by the uncertainties in the β values, and the LFs in the two bands are fully consistent with a constant QSO SED. As the number of sources in the M_{300} LF improves, with deeper near-IR photometry in the North and more complete spectroscopic coverage at faint z-band magnitudes in both hemispheres, the question of SED evolution will be an interesting one to revisit.

5.2 Redshift evolution and downsizing

Decades of survey work in the evolution of galaxies and QSOs have established a paradigm of cosmic downsizing: in this paradigm, the galaxies reaching the highest stellar masses have formed the bulk of their stars at high redshift during short epochs of particularly intense star formation; in contrast, galaxies of progressively lower mass formed at later cosmic epochs during more extended and less intense activity (e.g. Cowie et al. 1996, among many others). Given well-established relations between the mass of central supermassive black holes and the mass of their host galaxy bulges (Ferrarese & Merritt 2000; Kormendy & Ho 2013), we expect that the most massive black holes have thus grown most rapidly in the most luminous QSOs at high redshift. Surveys of QSOs have revealed a similar and matching trend of higher-luminosity objects peaking in activity at higher redshift, while lower-luminosity QSOs seem to have later activity peaks (e.g. Hasinger, Miyaji & Schmidt 2005; Hopkins, Richards & Hernquist 2007).

However, most of the past works could not draw on complete samples of QSOs at the extreme luminosities of $M_{145} < -28$, and hence we now compare the newest bright-end measurements of the QSO LF spanning the redshift range from $z \sim 4$ to $z \sim 6$ to reassess its evolution. In Fig. 7, we complement our work and that of

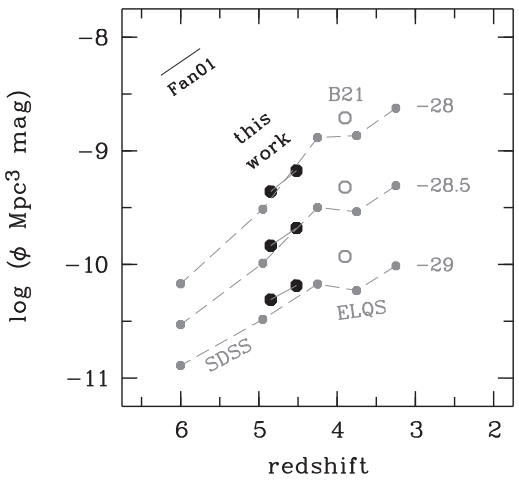

Figure 7. Evolution of $\Phi(M)$ with redshift at three M_{145} points. Large symbols are from Southern samples in the SkyMapper survey area, with black points from this work and the grey open symbol from Boutsia et al. (2021). Small points are dominated by Northern samples: Jiang et al. (2016) at $z \simeq 6$, Y16 at $z \simeq 5$ and ELQS (Schindler et al. 2019b) at $z < 4.5$. The Fan et al. (2001) evolution of dlog Φ^*/dz is shown in the top left corner.

W16/Y16 with the LFs from ELQS and from Boutsia et al. (2021) on the lower-z side and with the LF by Jiang et al. (2016) on the higher-z end. Here, we visualize space densities from the actual best-fitting parametrizations, because, due to the range of different bright-end slopes, it would be insufficient to consider only M^* and Φ^* parameters.

The evolution parameter of $\gamma = \mathrm{d}\log\Phi(M)/\mathrm{d}z = 0.47$ estimated by Fan et al. (2001) is shown in Fig. 7 as well and broadly consistent with the evolution at the highest redshifts. We see no strong evidence of a peak or plateau, although there is a hint of flattening around redshift 3–4.

6 SUMMARY

We continued our program to search for QSOs at $z \gtrsim 4$ in the Southern hemisphere using data from SkyMapper, *Gaia*, and several infrared surveys. We focus on the ultraluminous end of the QSO distribution, the luminosity range of $M_{145} < -27$ AB mag, where true QSOs are outnumbered by cool stars to the most extreme degree possible. In this paper, we extend the search area to an effective 14 486 deg^2. We have obtained full spectroscopic coverage of our candidate list at $z_{\rm PSF} < 18.7$ AB mag, at which depth we are >80 per cent complete.

We discover 126 new QSOs with $M_{145} < -27$ AB mag, on top of 21 such objects presented by Paper I, as well as a small number of less luminous objects. Previously, the most complete sample of bright high-redshift QSOs was that of W16 and Y16, found within a similarly sized search area in the Northern sky, with a focus on the redshift range of $4.7 < z < 5.4$.

We use our sample to redetermine the bright end of the QSO luminosity function at rest frame 145 nm, updating that of Y16, and also present for the first time the bright end of the high-redshift QSO luminosity function at rest frame 300 nm, capitalising on the depth of wide-field NIR photometry available in the Southern hemisphere.

We measure the slope of the M_{145} luminosity at $z = 4.7$–5.4 as $\beta = -3.38 \pm 0.32$ and -3.60 ± 0.37, depending on the faint-end constraint that is used, both of which are in line with several earlier estimates. In addition, we measure $\beta = -3.43 \pm 0.32$ for M_{300} from a fit with no faint-end constraint. In the $z = 4.4$–4.7 range, we measure slightly steeper bright-end slopes of $\beta = -3.53 \pm 0.24$ and -3.92 ± 0.32 for the M_{145} LF, and $\beta = -3.18 \pm 0.22$ for M_{300}.

A final determination of the QSO space densities at the luminous end and their evolution will require completing searches in the Northern hemisphere to create a complete all-sky sample of high-redshift QSOs. While this is one of our next steps, another is to push the completeness limit deeper to $z_{\rm PSF} \approx 19$ AB mag in order to obtain more robust statistics in the region where this sample connects to and overlaps with deeper literature samples. This, however, will require significant observational effort given that the contamination by stars increases with the fading discriminating power of *Gaia* parallaxes and proper motions at 19 AB mag and beyond.

ACKNOWLEDGEMENTS

A number of observers contributed spectroscopy of candidates through time-swapping arrangements or extreme generosity, and we thank them for their efforts: Harrison Abbot, Katie Auchettl, and Mike Bessell. We also thank the referee for suggestions that greatly improved the quality of the manuscript. CAO was supported by the Australian Research Council (ARC) through Discovery Project DP190100252. The national facility capability for SkyMapper has been funded through ARC LIEF grant LE130100104 from the Australian Research Council, awarded to the University of Sydney, the Australian National University, Swinburne University of Technology, the University of Queensland, the University of Western Australia, the University of Melbourne, Curtin University of Technology, Monash University and the Australian Astronomical Observatory. SkyMapper is owned and operated by The Australian National University's Research School of Astronomy and Astrophysics. The survey data were processed and provided by the SkyMapper Team at ANU. The SkyMapper node of the All-Sky Virtual Observatory (ASVO) is hosted at the National Computational Infrastructure (NCI). Development and support the SkyMapper node of the ASVO has been funded in part by Astronomy Australia Limited (AAL) and the Australian Government through the Commonwealth's Education Investment Fund (EIF) and National Collaborative Research Infrastructure Strategy (NCRIS), particularly the National eResearch Collaboration Tools and Resources (NeCTAR) and the Australian National Data Service Projects (ANDS). This project has made use of data from the European Space Agency (ESA) mission *Gaia* (https://www.cosmos.esa.int/gaia), processed by the *Gaia* Data Processing and Analysis Consortium (DPAC, https://www.cosmos.esa.int/web/gaia/dpac/consortium). Funding for the DPAC has been provided by national institutions, in particular the institutions participating in the *Gaia* Multilateral Agreement. This publication makes use of data products from the Wide-field Infrared Survey Explorer, which is a joint project of the University of California, Los Angeles, and the Jet Propulsion Laboratory/California Institute of Technology, and NEOWISE, which is a project of the Jet Propulsion Laboratory/California Institute of Technology. *WISE* and NEOWISE are funded by the National Aeronautics and Space Administration. We have used data products from the Two Micron All Sky Survey, which is a joint project of the University of Massachusetts and the Infrared Processing and Analysis Center/California Institute of Technology, funded by the National Aeronautics and Space Administration and the National Science Foundation. This paper uses data from the VISTA Hemisphere Survey ESO programme ID: 179.A-2010 (PI. McMahon). Based on observations obtained as part of the VISTA Hemisphere Survey, ESO Progam, 179.A-2010 (PI: McMahon). The VISTA Data Flow System pipeline processing and science archive are described in Irwin et al. (2004), Hambly et al. (2008) and Cross et al. (2012). This publication has made use of data from the VIKING survey from VISTA at the ESO Paranal Observatory, programme ID 179.A-2004. Data processing has been contributed by the VISTA Data Flow System at CASU, Cambridge and WFAU, Edinburgh. This research has made use of the SVO Filter Profile Service (http://svo2.cab.inta-csic.es/theory/fps/) supported from the Spanish MINECO through grant AYA2017-84089. The results presented here have utilised modules from the SCIPY software package (Jones et al. 2001).

DATA AVAILABILITY

The SMSS data underlying this article are available at the SkyMapper node of the All-Sky Virtual Observatory (ASVO), hosted at the National Computational Infrastructure (NCI) at https://skymapper.anu.edu.au. The data from SMSS Data Release 3 are currently accessible only to Australia-based researchers and their collaborators.

REFERENCES

Baldwin J. A., 1977, ApJ, 214, 679
Bessell M., Bloxham G., Schmidt B., Keller S., Tisserand P., Francis P., 2011, PASP, 123, 789
Boutsia K. et al., 2021, ApJ, 912, 111
Calderone G. et al., 2019, ApJ, 887, 268
Casagrande L., VandenBerg D. A., 2018, MNRAS, 479, L102
Chambers K. C. et al., 2016, preprint (arXiv:1612.05560)
Childress M. J., Vogt F. P. A., Nielsen J., Sharp R. G., 2014, Ap&SS, 349, 617
Cowie L. L., Songaila A., Hu E. M., Cohen J. G., 1996, AJ, 112, 839
Cross N. J. G. et al., 2012, A&A, 548, A119
Dopita M. et al., 2010, Ap&SS, 327, 245
Edge A., Sutherland W., Kuijken K., Driver S., McMahon R., Eales S., Emerson J. P., 2013, ESO Messenger, 154, 32
Fan X. et al., 2001, AJ, 121, 54

Ferrarese L., Merritt D., 2000, ApJ, 539, L9
Flesch E. W., 2015, PASA, 32, e010
Gaia Collaboration, 2018, A&A, 616, A1
Gaia Collaboration, 2021, A&A, 649, A1
Grazian A. et al., 2022, ApJ, 924, 62
Guarneri F.et et al., 2021, MNRAS, 506, 2471
Hambly N. C.et et al., 2008, MNRAS, 384, 637
Harikane Y. et al., 2022, ApJS, preprint (arXiv:2108.01090)
Hasinger G., Miyaji T., Schmidt M., 2005, A&A, 441, 417
Hinton S. R., Davis T. M., Lidman C., Glazebrook K., Lewis G. F., 2016, Astron. Comput., 15, 61
Hopkins P. F., Richards G. T., Hernquist L., 2007, ApJ, 654, 731
Irwin M. J.et et al., 2004, in Quinn P. J., Bridger A., eds, Proc. SPIE Conf. Ser. Vol. 5492, Optimizing Scientific Return for Astronomy through Information Technologies. SPIE, Bellingham, p. 411
Jiang L. et al., 2016, ApJ, 833, 222
Jones E. et al., 2001, SciPy: Open source scientific tools for Python. Available at: http://www.scipy.org/
Karachentsev I. D., Makarov D. I., Kaisina E. I., 2013, AJ, 145, 101
Kim Y.et et al., 2020, ApJ, 904, 111 (K20)
Kormendy J., Ho L. C., 2013, ARA&A, 51, 511
Lyke B. W.et et al., 2020, ApJS, 250, 8
Marocco F.et et al., 2021, ApJS, 253, 8
Marshall H. L., Tananbaum H., Avni Y., Zamorani G., 1983, ApJ, 269, 35
McGreer I. D.et et al., 2013, ApJ, 768, 105
McGreer I. D., Fan X., Jiang L., Cai Z., 2018, AJ, 155, 131
McMahon R. G., Banerji M., Gonzalez E., Koposov S. E., Bejar V. J., Lodieu N., Rebolo R., Collaboration VHS, 2013, The Messenger, 154, 35
Mortlock D. J., Patel M., Warren S. J., Hewett P. C., Venemans B. P., McMahon R. G., Simpson C., 2012, MNRAS, 419, 390
Nidever D. L.et et al., 2021, AJ, 161, 192
Niida M.et et al., 2020, ApJ, 904, 89 (N20)
Onken C. A.et et al., 2019, PASA, 36, 33
Onken C. A., Bian F., Fan X., Wang F., Wolf C., Yang J., 2020, MNRAS, 496, 2309
Rakshit S., Stalin C. S., Kotilainen J., 2020, ApJS, 249, 17
Reed S. L.et et al., 2017, MNRAS, 468, 4702
Richards G. T.et et al., 2009, AJ, 137, 3884
Riello M.et et al., 2021, A&A, 649, A3
Rodrigo C., Solano E., 2020, Contributions to the XIV.0 Scientific Meeting (virtual) of the Spanish Astronomical Society. Available at: https://www.sea-astronomia.es/reunion-cientifica-2020
Rodrigo C., Solano E., Bayo A., 2012, IVOA Working Draft. Available at: 10.5479/ADS/bib/2012ivoa.rept.1015R
Ryan-Weber E. V., Pettini M., Madau P., Zych B. J., 2009, MNRAS, 395, 1476
Schindler J.-T.et et al., 2019a, ApJS, 243, 5
Schindler J.-T.et et al., 2019b, ApJ, 871, 258
Schlafly E. F., Finkbeiner D. P., 2011, ApJ, 737, 103
Schlegel D. J., Finkbeiner D. P., Davis M., 1998, ApJ, 500, 525 (SFD)
Selsing J., Fynbo J. P. U., Christensen L., Krogager J.-K., 2016, A&A, 585, A87
Simcoe R. A.et et al., 2011, ApJ, 743, 21
Skrutskie M. F.et et al., 2006, AJ, 131, 1163
Telfer R. C., Zheng W., Kriss G. A., Davidsen A. F., 2002, ApJ, 565, 773
Vanden Berk D. E.et et al., 2001, AJ, 122, 549
Wang S., Chen X., 2019, ApJ, 877, 116
Wang F.et et al., 2016, ApJ, 819, 24 (W16)
Wenzl L.et et al., 2021, AJ, 162, 72 (W21)
Wolf C., Meisenheimer K., Röser H.-J., 2001, A&A, 365, 660
Wolf C.et et al., 2018a, PASA, 35, 10
Wolf C., Bian F., Onken C. A., Schmidt B. P., Tisserand P., Alonzi N., Hon W. J., Tonry J. L., 2018b, PASA, 35, 24
Wolf C.et et al., 2020, MNRAS, 491, 1970 (Paper I)
Wright E. L.et et al., 2010, AJ, 140, 1868
Xie X., Shao Z., Shen S., Liu H., Li L., 2016, ApJ, 824, 38
Yang J. et al., 2016, ApJ, 829, 33(Y16)
Yang J. et al., 2017, AJ, 153, 184
Yang J. et al., 2019, ApJ, 871, 199
York D. G.et et al., 2000, AJ, 120, 1579

APPENDIX A: SPECTRUM GALLERY

In the figures below, we present the WiFeS spectra for the newly discovered QSOs from the redshift range $z = 3.8$–5.5, ordered by RA.

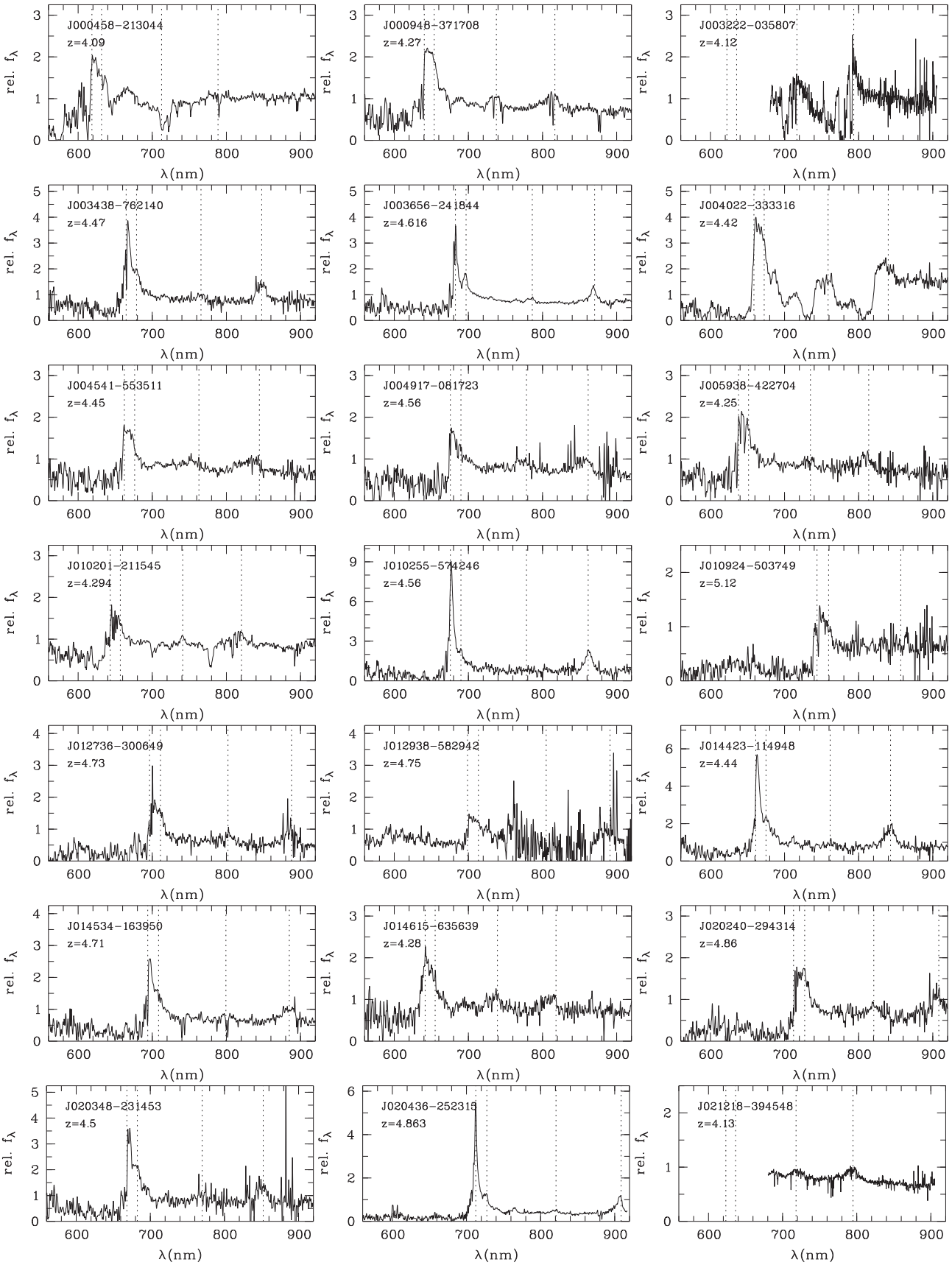

Figure A1. Gallery of $3.8 > z > 5.5$ QSO spectra obtained in this work, ordered by RA, page 1. Vertical dashed lines indicate the wavelengths of Ly α, N V, Si IV, and C IV at our adopted redshift.

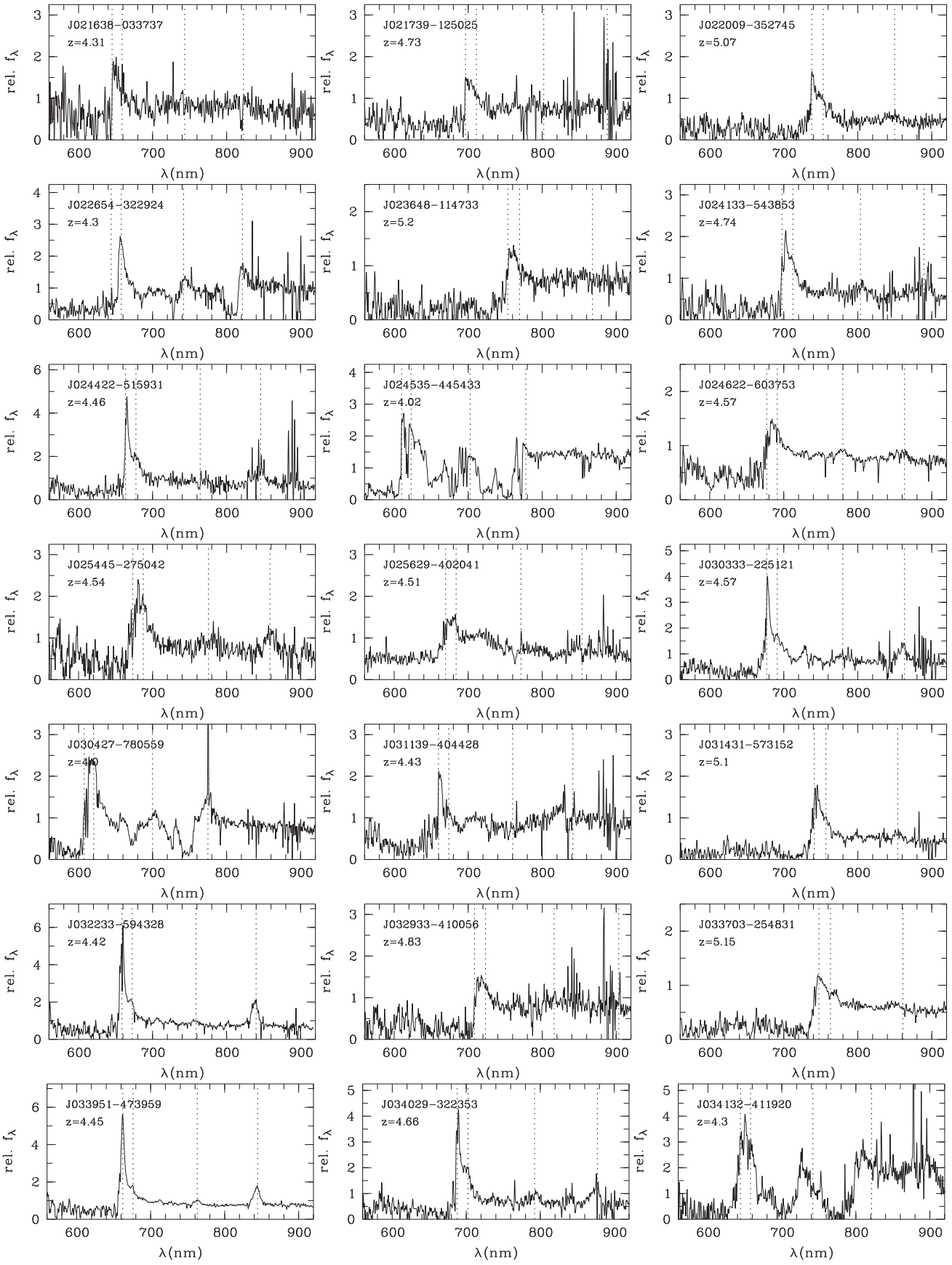

Figure A2. Gallery of $3.8 > z > 5.5$ QSO spectra obtained in this work, ordered by RA, page 2.

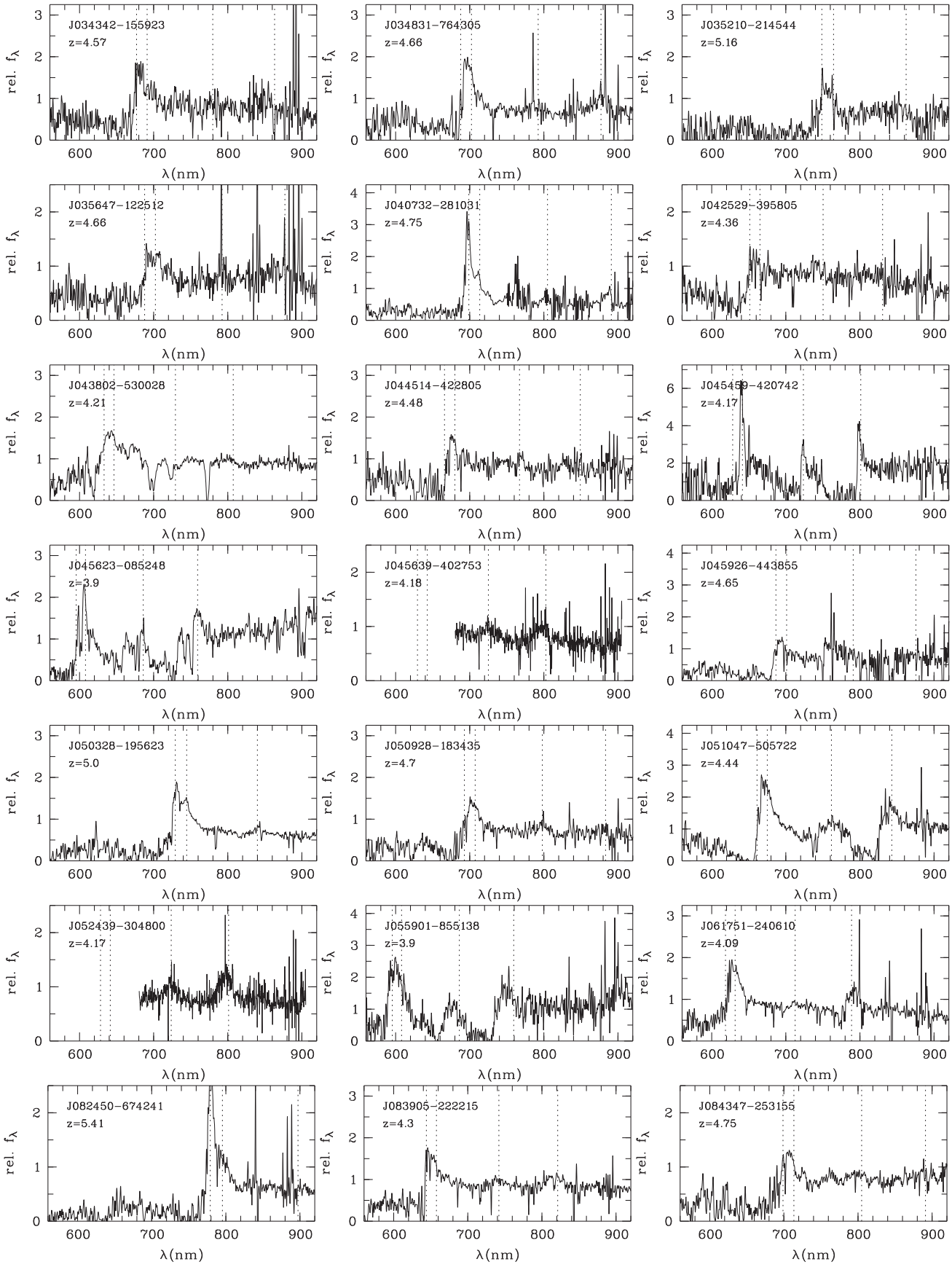

Figure A3. Gallery of $3.8 > z > 5.5$ QSO spectra obtained in this work, ordered by RA, page 3.

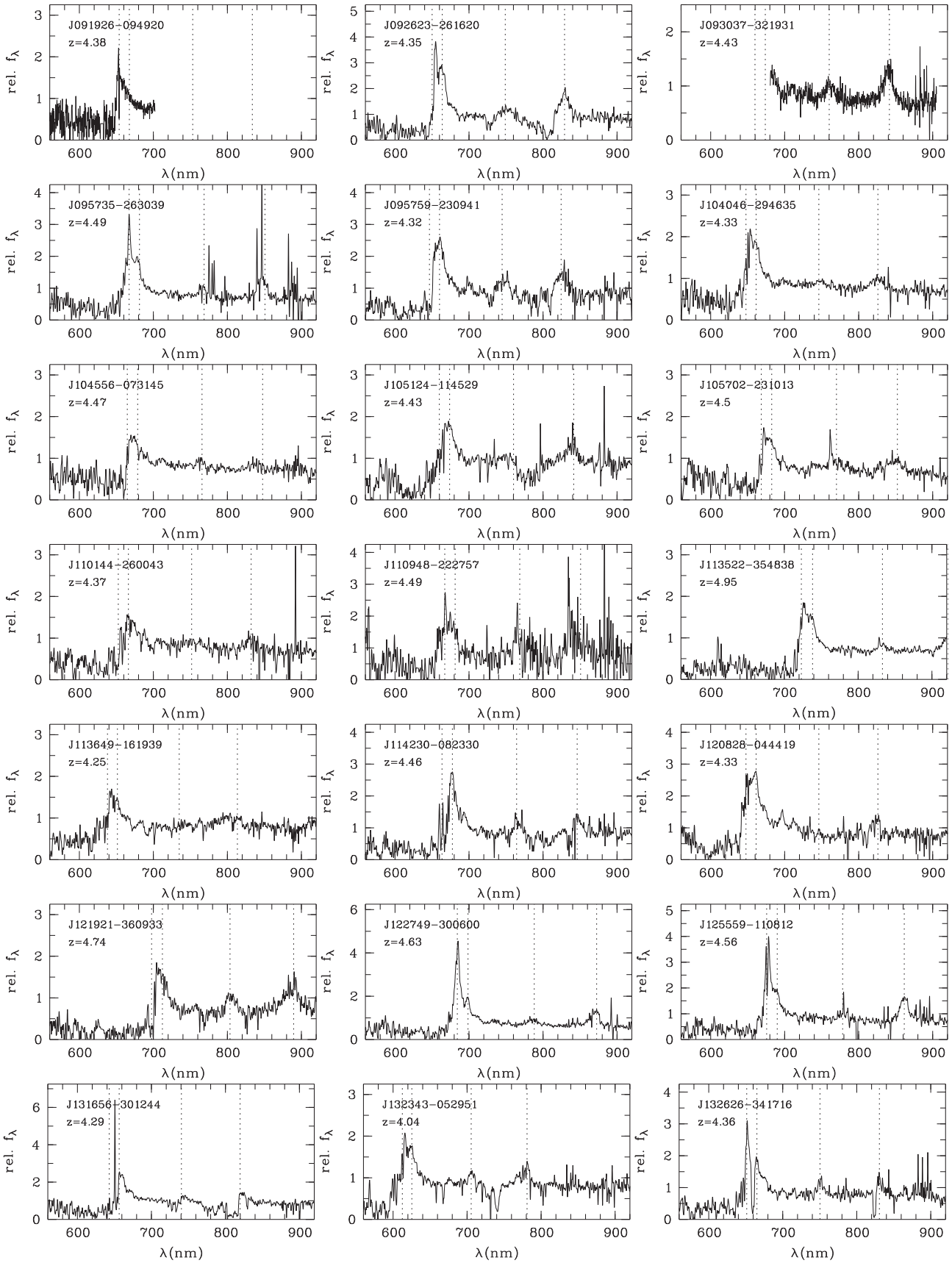

Figure A4. Gallery of $3.8 > z > 5.5$ QSO spectra obtained in this work, ordered by RA, page 4.

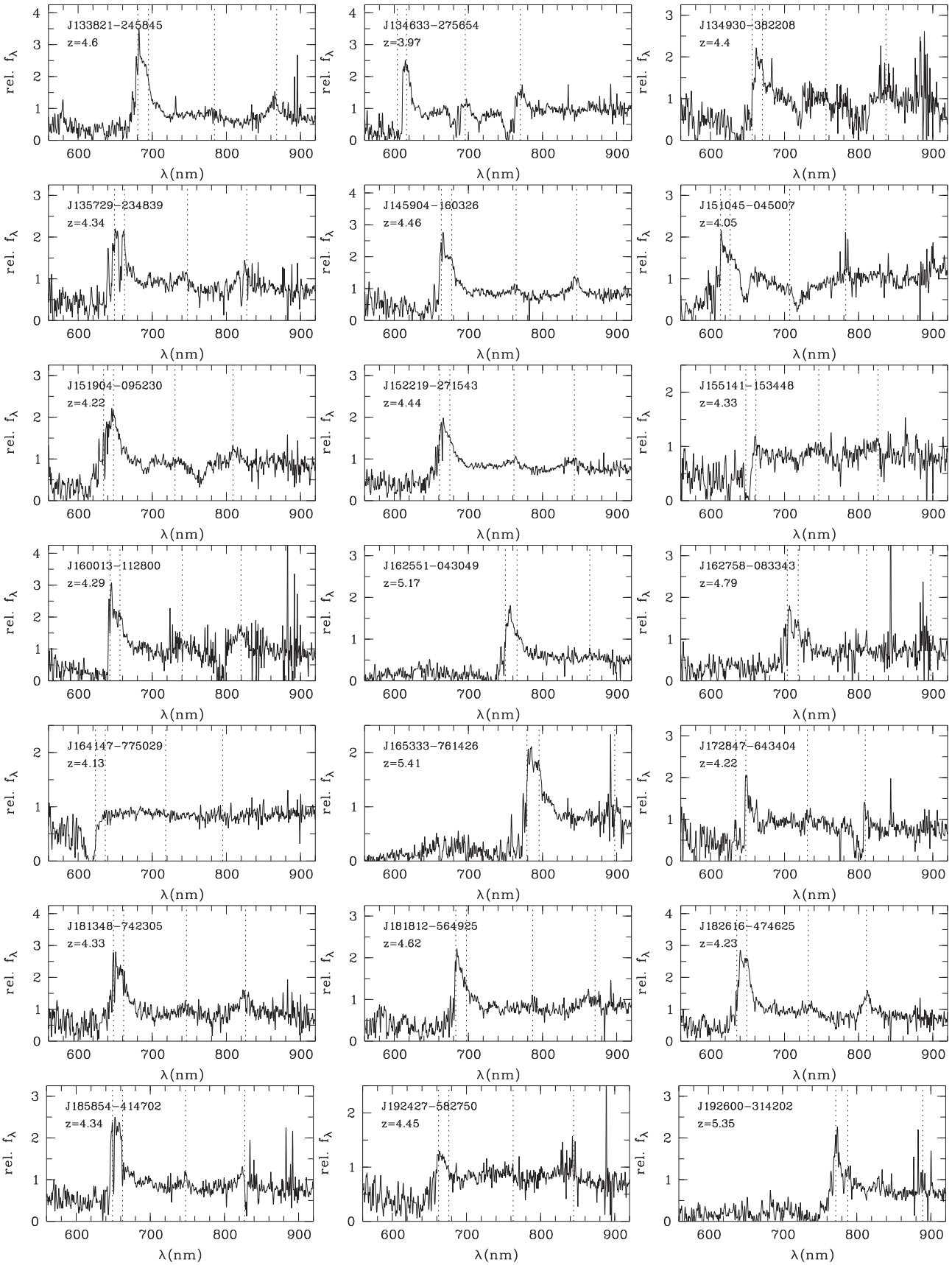

Figure A5. Gallery of $3.8 > z > 5.5$ QSO spectra obtained in this work, ordered by RA, page 5.

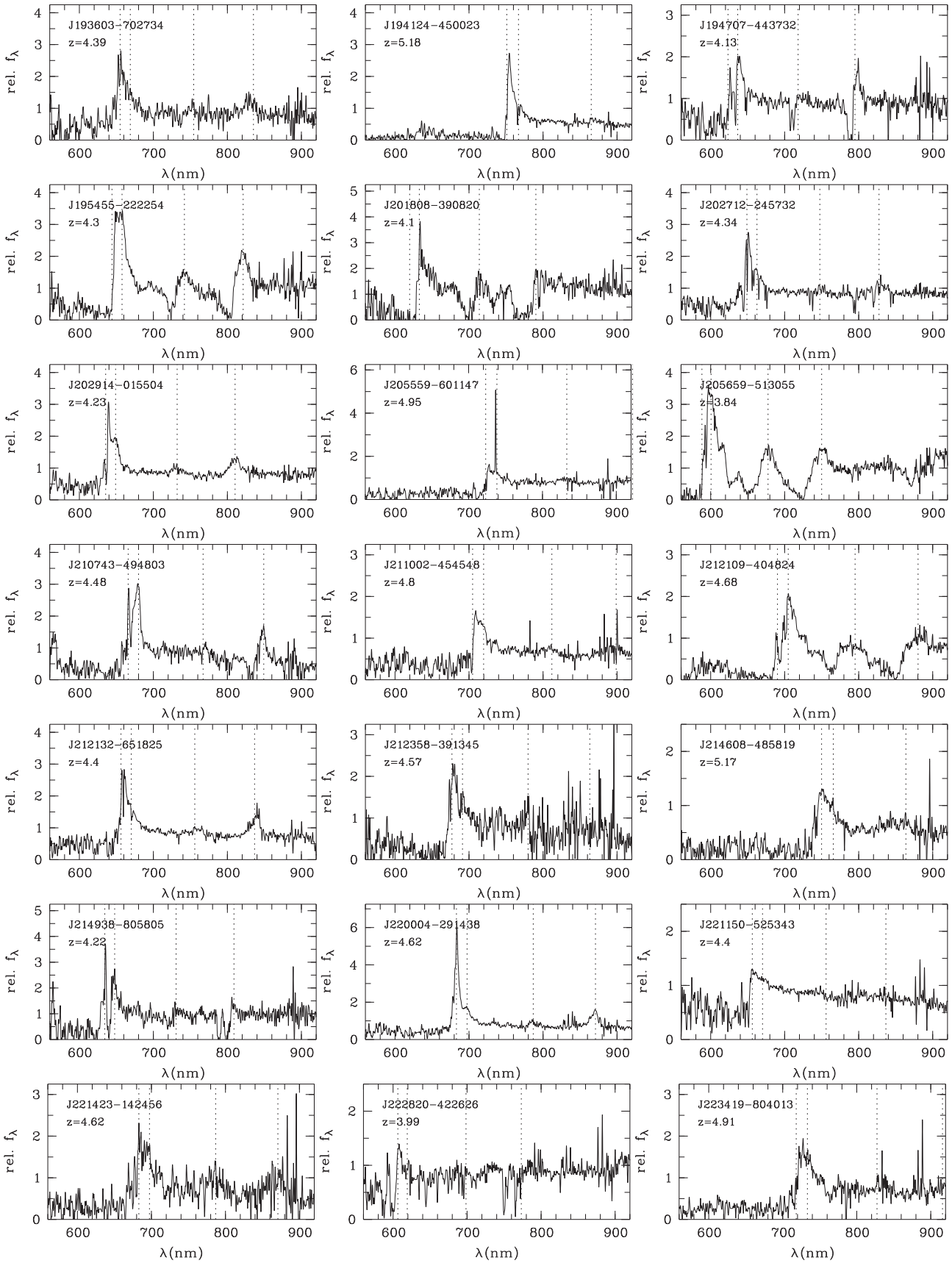

Figure A6. Gallery of $3.8 > z > 5.5$ QSO spectra obtained in this work, ordered by RA, page 6.

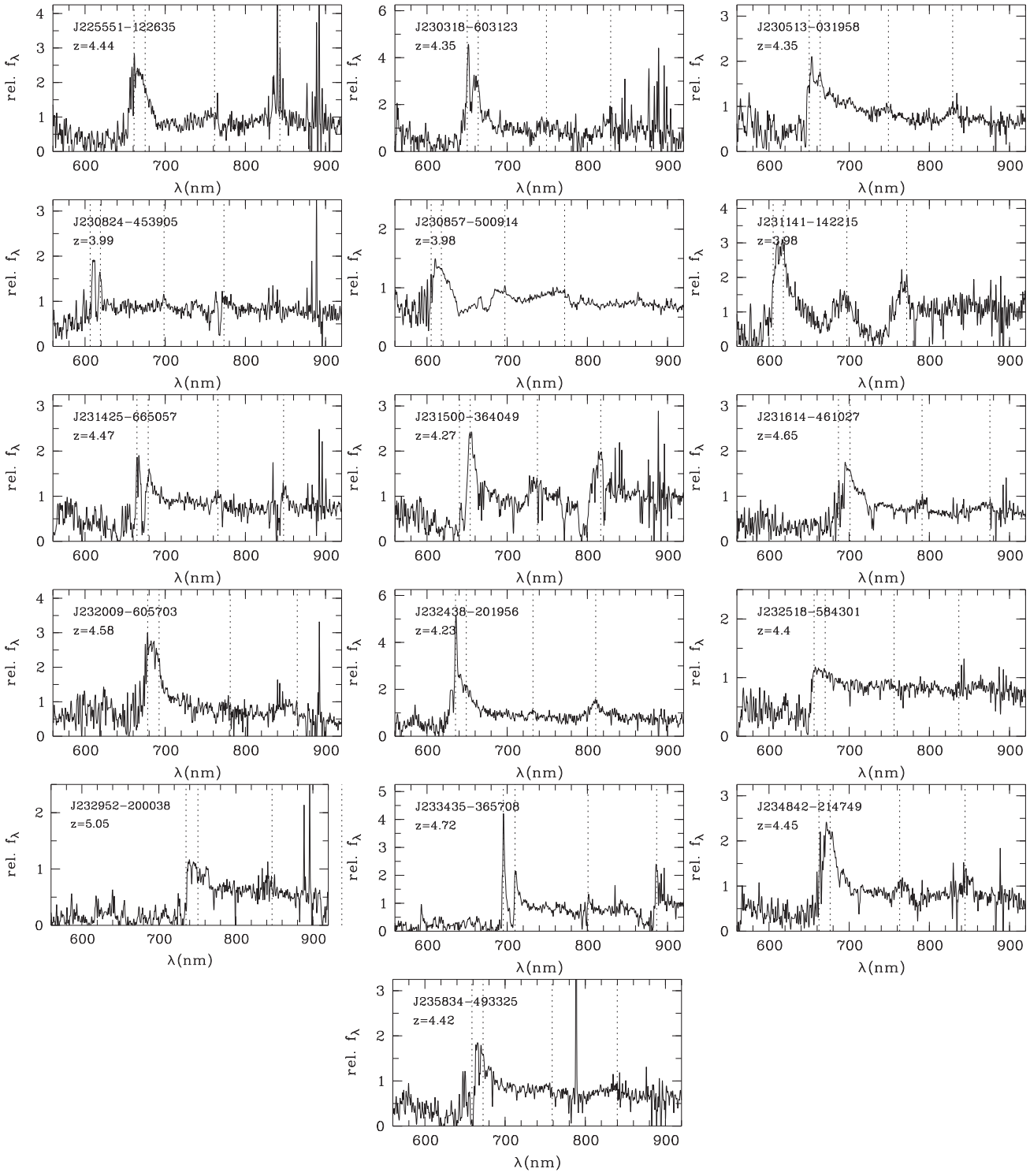

Figure A7. Gallery of $3.8 > z > 5.5$ QSO spectra obtained in this work, ordered by RA, page 7.

APPENDIX B: SMSS J164147.78−775029.8

The lack of prominent emission lines in SMSS J164147.78–775029.8 led us to acquire additional WiFeS spectroscopy with the RT480 beam-splitter on UT 2021-07-04, in an attempt to better examine the associated Ly α forest absorption and confirm the redshift. We present the weighted average spectrum in Fig. B1, with a 3-pixel median smoothing applied to reduce the noise. The onset of absorption shortward of Ly α and the lack of transmitted flux shortward of the Lyman limit lend confidence to the inferred redshift of 4.13.

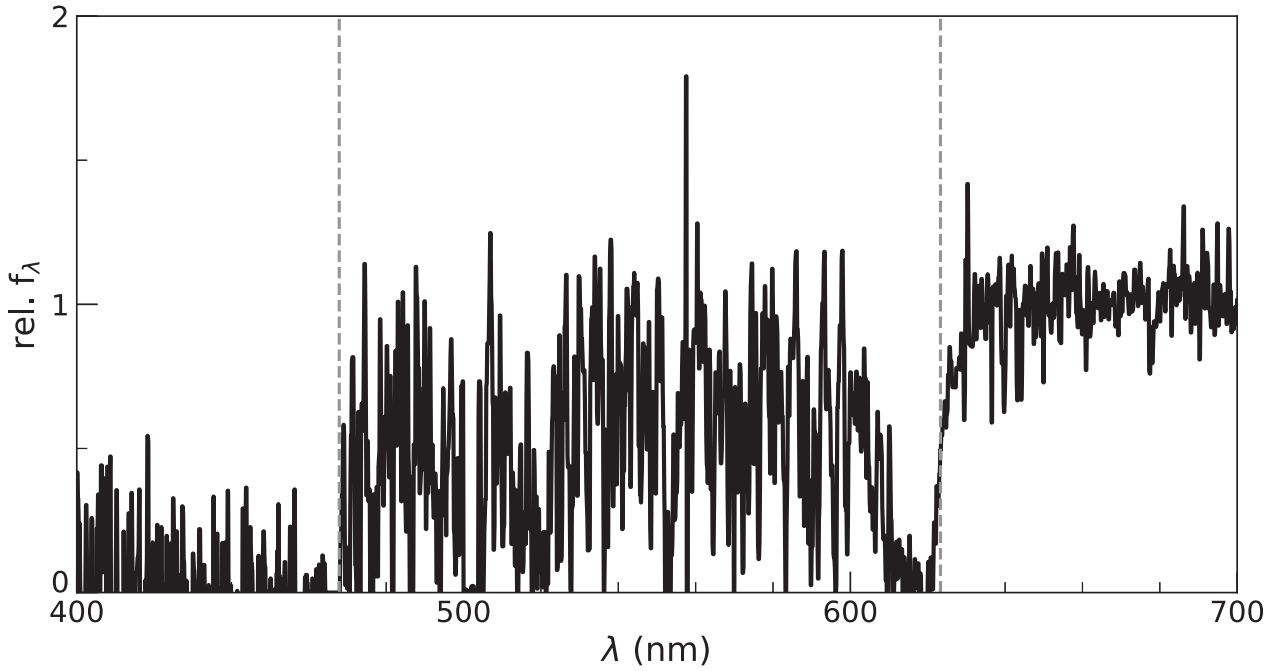

Figure B1. Coadded observed-frame WiFeS spectrum of SMSS J164147.78−775029.8 obtained with two different beam-splitters to better cover the wavelength range between Ly α and the Lyman limit (shown as the two dashed vertical lines for our adopted redshift of $z = 4.13$.).

This paper has been typeset from a TEX/LATEX file prepared by the author.